Astronomy & Astrophysics manuscript no. ms
December 8, 2017

The AMBRE project: The thick thin disk and thin thick disk of the Milky Way

M. R. Hayden[1], A. Recio-Blanco[1], P. de Laverny[1], S. Mikolaitis[2], C. C. Worley[3]

(Affiliations can be found after the references)

December 8, 2017

ABSTRACT

We analyze 494 main sequence turnoff and subgiant stars from the AMBRE:HARPS survey. These stars have accurate astrometric information from *Gaia*/DR1, providing reliable age estimates with relative uncertainties of ±1 or 2 Gyr and allowing precise orbital determinations. The sample is split based on chemistry into a low-[Mg/Fe] sequence, which are often identified as thin disk stellar populations, and a high-[Mg/Fe] sequence, which are often associated with thick disk stellar populations. We find that the high-[Mg/Fe] chemical sequence has extended star formation for several Gyr and is coeval with the oldest stars of the low-[Mg/Fe] chemical sequence; both the low- and high-[Mg/Fe] sequences were forming stars at the same time. We find that the high-[Mg/Fe] stellar populations are only vertically extended for the oldest, most-metal poor and highest [Mg/Fe] stars. When comparing vertical velocity dispersion for the low- and high-[Mg/Fe] sequences, the high-[Mg/Fe] sequence has lower vertical velocity dispersion than the low-[Mg/Fe] sequence for stars of similar age. This means that identifying either group as thin or thick disk based on chemistry is misleading. The stars belonging to the high-[Mg/Fe] sequence have perigalacticons that originate in the inner disk, while the perigalacticons of stars on the low-[Mg/Fe] sequence are generally around the solar neighborhood. From the orbital properties of the stars, the high-[Mg/Fe] and low-[Mg/Fe] sequences are most likely a reflection of the chemical enrichment history of the inner and outer disk populations, respectively; radial mixing causes both populations to be observed in situ at the solar position. Based on these results, we emphasize that it is important to be clear in defining what populations are being referenced when using the terms thin and thick disk, and that ideally the term thick disk should be reserved for purely geometric definitions to avoid confusion and be consistent with definitions in external galaxies.

Key words. Galaxy:disk, Galaxy:structure, Galaxy:evolution, Galaxy:abundances, Galaxy:stellar content

1. Introduction

Unraveling the chemodynamic structure of the Milky Way is a key constraint for models of chemical and galaxy evolution. However, there has been much debate over the current structure of the disk (e.g., Rix & Bovy 2013), in which the interplay between the thin and thick disks is unclear. The advent of high-resolution spectroscopic surveys, along with data from the *Gaia* (Prusti et al. 2016; Brown et al. 2016) satellite, has the potential to unravel the current mysteries surrounding the formation and evolution of the Milky Way disk.

The thick disk was first identified by Yoshii (1982); Gilmore & Reid (1983) as an overdensity of stars at large distances from the Galactic plane. The stars of the thick disk in the solar neighborhood have been found to be α-enhanced relative to the Sun (e.g., Fuhrmann 1998; Bensby et al. 2003; Adibekyan et al. 2013; Recio-Blanco et al. 2014) and subsolar metallicity at around -0.5 dex. More recent observations have led to the discovery of intermediate α populations at much higher metallicities (e.g., Bensby et al. 2007; Adibekyan et al. 2011; Hayden et al. 2015; Mikolaitis et al. 2017), although there may be a prominent gap between the metal-poor high-[Mg/Fe] populations and the more metal-rich intermediate-[Mg/Fe] populations (e.g., Adibekyan et al. 2011). The origin of these intermediate-[Mg/Fe] populations is difficult to discern. It is possible that they are chemically related to the high-[Mg/Fe] metal-poor stars (e.g., Haywood et al. 2016), are a distinct population (e.g., Jofré et al. 2017), or could also result from extra mixing along the RGB for metal-rich populations (Masseron & Gilmore 2015). If the high-[Mg/Fe] metal-poor stars are chemically related with the intermediate-[Mg/Fe] stars, there appears to be two distinct stellar population sequences in the solar neighborhood. One sequence starts at high-[Mg/Fe] with the [Mg/Fe] decreasing as [Fe/H] increases even past solar metallicities, and one sequence begins at solar-[Mg/Fe] abundances spanning a wide range of metallicities from $\sim -0.6 <$ [Fe/H] < 0.4. The thick and thin disks are often identified in the [Mg/Fe] versus [Fe/H] plane chemically; these intermediate-α high-metallicity stars are sometimes lumped in with the thick disk populations and the solar-[Mg/Fe] populations are identified with the thin disk. However, the connections, if there are any, between the thin and thick disk chemical sequences is unclear. Furthermore, there is overlap between the sequences at the highest metallicities at solar-[Mg/Fe] abundances and it is also uncertain to which sequence (or both) these stellar populations belong. It has been argued that what we identify as the thick disk in the chemical plane is not a distinct phase of the disk evolution, but is instead the chemical evolution track of stellar populations from the inner Galaxy that is brought to the solar neighborhood through radial mixing processes (Haywood et al. 2013). In this case, it is likely that the super solar-metallicity populations currently identified as thin disk are actually the metal-rich extension of the high-[Mg/Fe] thick disk sequence.

With the advent of precision astrometric measurements from *Gaia*, we can now measure accurately ages, velocities, and orbital properties for large numbers of stars that can be used in conjunction with ground-based spectroscopic surveys. In this paper, we describe the AMBRE:HARPS dataset of main sequence turnoff (MSTO)/subgiant stars for which we obtain reliable ages and measure the chemical, kinematic, and temporal properties of the disk. We then discuss the structure of the disk in the solar neighborhood based on the HARPS-TGAS dataset.

2. Data

2.1. AMBRE:HARPS

The AMBRE project is a uniform analysis of high-resolution archival ESO spectra, as described in de Laverny et al. (2013). We focused on spectra taken from the HARPS instrument as this sample has large overlap with the *Gaia*/TGAS catalog. Stellar parameters are derived using the MATISSE algorithm (Recio-Blanco et al. 2006), as described in De Pascale et al. (2014) for the HARPS instrument. Individual abundances for this sample are derived in Mikolaitis et al. (2017). In particular, our analysis uses the effective temperature measurements from AMBRE, along with the [Fe/H] and [Mg/Fe] derived in the Mikolaitis et al. (2017) analysis. Typical errors are < 100K in $T_{\rm eff}$ and 0.05 dex in [Fe/H] and [Mg/Fe].

2.2. Gaia DR1

Parallaxes and proper motions for the AMBRE:HARPS sample were taken from *Gaia* DR1 (Lindegren et al. 2016). This sample is hereafter referred to as HARPS-TGAS and contains $\sim$ 1500 stars. We computed distances using a Bayesian approach as outlined in Bailer-Jones (2015), consisting of a single disk with an exponential scale height of 300 pc and exponential scale length of 2.7 kpc. Additionally, we used the luminosity function derived by Robin et al. (2012). As the majority of the sample is within 50 pc, the choice of prior has little impact on the overall results, as the fractional parallax error at these distances is very small ($< 5\%$).

2.3. Ages

We used Bayesian inference to determine ages for the HARPS-TGAS sample using methods similar to those described in (Jørgensen & Lindegren 2005) by comparing the derived stellar parameters to Dartmouth isochrones (Dotter et al. 2008; http://stellar.dartmouth.edu/models/isolf_new.html). We select main sequence turnoff and subgiant stars for which the age estimates are most reliable. A more detailed description of the ages is given in Appendix A. The average (1σ) relative errors for the ages are 1-2 Gyr when using simulated observations from TRILEGAL Girardi et al. (2005) or comparing to the sample analyzed by Haywood et al. (2013). The isochrones range in age from 0 to 15 Gyr, so the absolute age scale used in this analysis is somewhat stretched, particularly for the oldest stars.

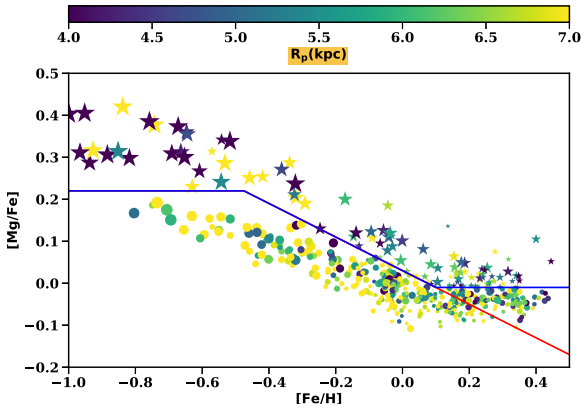

Fig. 1. [Mg/Fe] vs. [Fe/H] plane for the HARPS sample with reliable age estimates. The blue line denotes our chemical separation between thin and thick disks, where the thick disk stars (star symbol) are shown above the line and thin disk stars (circle symbol) below the line. The size of each data point denotes the relative age of each star; the larger points are older than smaller points. Stars are color coded by their R_p . The color bar stops at $R_p = 7$ kpc to prevent color saturation of stars coming from the inner Galaxy. Which sequence the most metal-rich, solar-[Mg/Fe] stars belong to is unclear, and we show the red line as an example of a different potential split between stellar population groups.

2.4. Velocities and orbits

Velocities and orbits were determined via *Galpy* (Bovy 2015) using distances and proper motions from *Gaia* DR1, along with radial velocities as determined by *AMBRE*. For the orbit integration, we used the MWPotential2014 described in Bovy (2015) for the Galactic potential. We assume a solar position of 8 kpc and a rotational velocity of the disk of 220 km s^{-1} . Typical uncertainties in individual velocity components are $\lesssim$1 km s^{-1} and in the orbital parameters such as R_p or z_{max} of $\sim 5\%$. Errors in the velocities and orbital parameters are computed using a Monte Carlo (MC) of the dervied and observed parameters (e.g., $T_{\rm eff}$, M_K, μ). The method for measuring the vertical velocity dispersion is described in Guiglion et al. (2015) and Hayden (2017a). We measured the vertical velocity dispersion in bins of 2 Gyr and required a minimum of eight stars per bin to compute the velocity measurements.

3. Results

3.1. Ages of the thin and thick disk stars

We separated the stars into low- and high-[Mg/Fe] sequences based on a combination of their [Mg/Fe] and [Fe/H] abundances as shown by the blue line in Fig. 1; the high-[Mg/Fe] stars (star symbols) represent those above the blue line, while the low-[Mg/Fe] stars (circles) represent those below the blue line. Individual stars are color coded by the estimated perigalacticon R_p. The R_p is the closest approach to galactic center of the orbit of a star and is a useful tracer, particularly for the most metal-rich populations, in constraining the relative importance of the different mechanisms responsible for radial mixing of stellar populations (i.e., blurring versus churning; see Sellwood & Binney 2002). The color bar has a cutoff of $R_p = 7$ kpc, but many

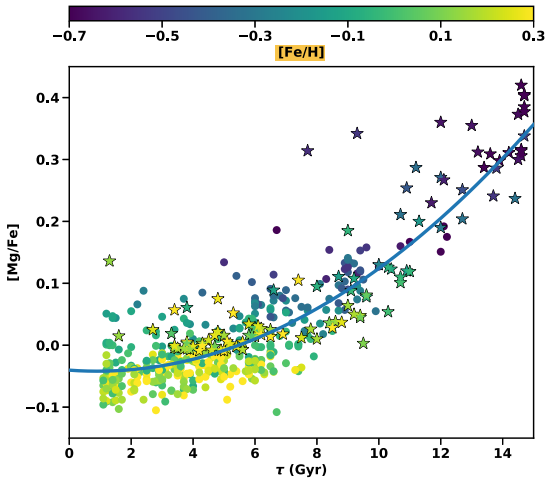

Fig. 2. [Mg/Fe] vs. age relation for the HARPS sample, with stars color-coded by metallicity. The symbols used are the same as in Fig. 1, where the high-[Mg/Fe] track is represented by stars and the low-[Mg/Fe] track as circles.

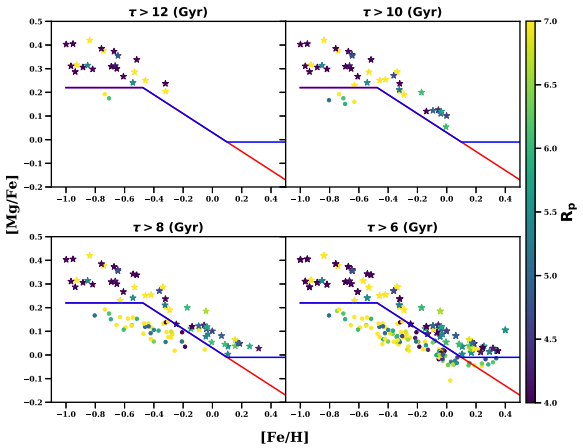

Fig. 3. [Mg/Fe] vs. [Fe/H] plane as a function of various age ranges, going from oldest to younger stellar populations. Stars are color coded by their perigalacticons R_p. The blue and red lines are the same as in Fig. 1, where the high-[Mg/Fe] population are denoted by star symbols and the low-[Mg/Fe] population are denoted by circles.

of the stars actually have larger R_p that extend all the way to the solar radius at $\sim$ 8 kpc. The cutoff prevents color saturation of the stars belonging to the inner disk.

In Fig. 2 we find that the oldest stellar populations, with $\tau > 12$ Gyr, belong to the high-[Mg/Fe] sequence (star symbols) and are the most metal-poor and high-α stars in the sample. Many of these stars come from the inner Galaxy, with $R_p < 5$ kpc (Fig. 1), and are likely associated with the classical thick disk. We find that there is extended star formation for many Gyr along the high-[Mg/Fe] sequence, as shown in Fig. 3. Following the high-[Mg/Fe] track, we find that the [Mg/Fe] ratio begins to decrease at [Fe/H]~ -0.5, as Type Ia supernovae begin to pollute the ISM. As shown in Fig. 1 and 2 there is a clear age-α-metallicity relation for the thick disk stars up until $\tau \sim 6$ Gyr ([Fe/H]$\sim$ 0.2), where the [Mg/Fe] ratio decreases and metallicity increases for younger stellar populations. For stars along the high-[Mg/Fe] sequence, we see a general trend in increasing R_p with increasing metallicity: that is to say, the orbits for younger stars along the high-[Mg/Fe] sequence are more circular than those of older high-[Mg/Fe] stars. It is unclear to which stellar populations the most metal-rich solar-[Mg/Fe] stars belong: it is possible that the stars with [Fe/H]$>$ 0.2 that are currently labeled as thin disk are in fact the most metal-rich extension of the high-[Mg/Fe] chemical track. As an example, the red line in Fig. 1 shows a different potential split between stellar populations for which the highest metallicity populations all belong to the high-[Mg/Fe] sequence. In this case, star formation along the thick disk sequence has continued up to present day.

Along the low-[Mg/Fe] track, we find that the oldest stars appear $\sim$ 10 Gyr ago at intermediate [Mg/Fe] abundances and low (< -0.6 dex) metallicity. We define a star as having a roughly circular orbit if it has $e < 0.2$. We find that many of these older thin disk stars are on circular orbits in the solar neighborhood or come from larger radii with apogalacticons greater than 10 kpc; very few of such thin disk stars are on orbits that stray into the inner disk. The thin disk sequence has a slight τ -α-metallicity relation for older, more metal-poor populations. As age increases, α decreases and metallicity decreases. However, this relationship breaks down at around $\sim$ 6 Gyr, as stars with these ages have a large range in metallicity. For $\tau < 6$ Gyr, there is a spread for $-0.5 <$ [Fe/H] < 0.4 in metallicity: for these stars there is no age-α-metallicity relation and there is a large dispersion in the derived metallicities for the youngest stellar populations. For the most metal-rich stars on the thin disk track ([Fe/H]$> 0.1 - 0.2$), we find that more than half are on circular orbits ($e < 0.2$), despite their likely origin in the inner Galaxy based on their high metallicities.

Finally, we find significant age overlap between the low- and high-[Mg/Fe] sequences for many Gyr between $\sim 6 < \tau < 10$ Gyr: the stellar populations belonging to the low- and high-[Mg/Fe] populations are coeval and both tracks formed stars of very different metallicities at the same time, as shown in Fig. 3.

3.2. Vertical distribution of the low- and high-[Mg/Fe] tracks

Using bins of 2 Gyr, we measured the vertical velocity dispersion for both the low- (green line) and high-[Mg/Fe] (blue line) sequences as shown in Fig. 4. We find little evidence for a step function in the vertical velocity dispersion, and instead find that the vertical velocity dispersion generally smoothly increases with age for both tracks, save for a dip at $\tau \sim 8$ Gyr for the older thin disk stars. This means that the high-[Mg/Fe] sequence is only vertically extended for the oldest, highest [Mg/Fe] populations and the vertical extent of the high-[Mg/Fe] stars drops rapidly with age. Most striking is that the velocity dispersion for the high-[Mg/Fe] track is, at the same age, always equal to or lower than the low-[Mg/Fe] track. The high-[Mg/Fe] sequence is no more vertically extended than the low-[Mg/Fe] sequence when the populations are coeval.

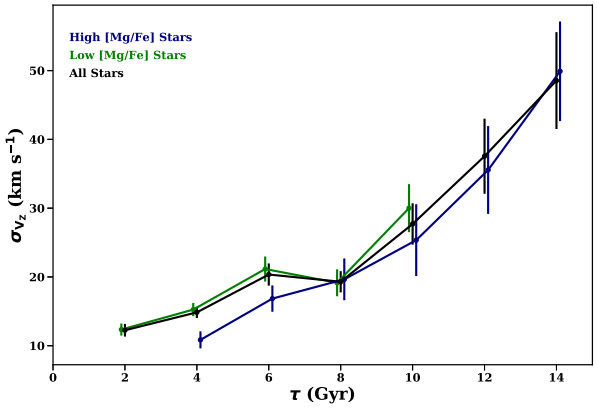

Fig. 4. Vertical velocity dispersion as a function of age for the low-[Mg/Fe] (green), high-[Mg/Fe] (blue), and total (black) stellar sample. Velocity dispersion is measured in bins of 2 Gyr, where each bin has a minimum of 8 stars per bin.

4. Discussion

We find that the high-[Mg/Fe] sequence has an extended star formation history, potentially up to the present day and that the low- and high-[Mg/Fe] sequences have significant age overlap and are coeval. Chemically, there are two distinct sequences forming stars at the same time at vastly different metallicities. The high-[Mg/Fe] sequence is traditionally identified with the thick disk, but is only vertically extended for the oldest, highest [Mg/Fe] , most metal-poor populations. At the ages where the low- and high-[Mg/Fe] sequences overlap, there is little difference in the vertical heights of the two populations.

We also note that our results could be dependent on the selection function for the AMBRE:HARPS sample. However, these results have been observed previously by Bovy et al. (2012) and Bovy et al. (2016), using SEGUE and APOGEE data, respectively, but were not commented on extensively in these papers. Additionally, we note that any large errors in age determination could cause an error in the measurement of the velocity dispersion.

What we are likely seeing is the mixing of two stellar populations coming from different locations: the high-[Mg/Fe] sequence, which formed in the inner Galaxy where star formation rates were significantly higher than the low-[Mg/Fe] sequence, which formed stars at much lower rates and had a more gradual build up of metallicity. Stars belonging to the high-[Mg/Fe] sequence are observed in the solar neighborhood via radial mixing, wherein the older stars are primarily blurred to the solar cylinder, while those of higher metallicity and lower [Mg/Fe] come from both blurring and churning mechanisms. The idea that the solar neighborhood is the juxtaposition of the inner and outer disk is not new. Haywood et al. (2013) argued that this is a potential explanation for the observations of the two sequences in the solar neighborhood, and the potential mixing of the high-[Mg/Fe] sequence with a more in situ population was initially seen in Fig. 20 of Edvardsson et al. (1993), who found that stars coming from the inner disk were often metal poor and [Mg/Fe] enhanced, while more in situ stars generally had solar type abundances. Qualitatively, our results are very similar to those of Edvardsson et al. (1993) with respect to the inner disk being dominated by high-[Mg/Fe] populations. With the addition of extremely precise kinematics and distances from *Gaia* and a larger sample size of stars with reliable ages, we find that the high-[Mg/Fe] sequence was likely not a completely separate phase of disk evolution but indeed formed stars for many Gyr and was coeval with the the low-[Mg/Fe] sequence of populations. This inner disk origin for the bulk of the high-[Mg/Fe] sequence explains the relative similarity of the high-[Mg/Fe] sequence with radius (e.g., Nidever et al. 2014), as radially mixing of the high-[Mg/Fe] population out to larger radii preserves its appearance in the chemical plane.

Turning our attention to the super solar-metallicity populations, many of these stars are on circular orbits and never reach the radii at which they likely formed based on their high metallicity and the observed radial abundance gradients in the disk (e.g., Hayden et al. 2014). For these populations, churning is an important mechanism for bringing them to the solar neighborhood, which is in agreement with observations from Kordopatis et al. (2015) and Hayden (2017a). If we consider the super-solar metallicity stars as the metal-rich extension of the high-[Mg/Fe] sequence, the relative importance of various mixing processes for the high-[Mg/Fe] sequence depends on the age/metallicity of the stellar populations: older (more metal-poor) populations are most likely observed in the solar neighborhood via blurring, while the younger (more metal-rich) populations appear to be radially mixed via churning.

Based on these arguments, we find that the current chemical definitions of thin and thick disk are misleading. We urge that the term thick disk be reserved for the geometric thick disk, with the realization that the chemistry of stars making up the geometric thick disk vary depending on the radius at which they are observed. In the inner Galaxy and solar neighborhood, the geometric thick disk is dominated by metal-poor high-[Mg/Fe] populations, however in the outer disk the geometric thick disk is dominated by flaring solar-[Mg/Fe] populations (e.g., Hayden et al. 2015; Minchev et al. 2015; Bovy et al. 2016; Mackereth et al. 2017). Chemically, the two sequences observed in the [Mg/Fe] plane in the solar neighborhood are mostly likely a reflection of their birth radius, rather than a thin or thick disk, and the sequences are coeval. Inner and outer disk stellar populations is a less ambiguous definition for these sequences, as we have shown that calling the high-[Mg/Fe] sequence the chemical thick disk is a misleading and these populations are no thicker than the chemical thin disk for stars of the same age.

Acknowledgements. The authors thank Misha Haywood for providing derived ages from their 2013 paper and for useful discussions. MRH and ARB received financial support from ANR, reference 14-CE33-0014-01. This work has made use of data from the European Space Agency (ESA) mission *Gaia* (`https://www.cosmos.esa.int/gaia`), processed by the *Gaia* Data Processing and Analysis Consortium (DPAC; `https://www.cosmos.esa.int/web/gaia/dpac/consortium`). Funding for the DPAC has been provided by national institutions, in particular the institutions participating in the *Gaia* Multilateral Agreement.

References

Adibekyan, V. Z., Figueira, P., Santos, N. C., et al. 2013, A&A, 554, A44
Adibekyan, V. Z., Santos, N. C., Sousa, S. G., & Israelian, G. 2011, A&A, 535, L11

Bailer-Jones, C. A. L. 2015, PASP, 127, 994
Bensby, T., Feltzing, S., & Lundström, I. 2003, A&A, 410, 527
Bensby, T., Zenn, A. R., Oey, M. S., & Feltzing, S. 2007, ApJ, 663, L13
Bovy, J. 2015, ApJS, 216, 29
Bovy, J., Rix, H.-W., Hogg, D. W., et al. 2012, ApJ, 755, 115
Bovy, J., Rix, H.-W., Schlafly, E. F., et al. 2016, ApJ, 823, 30
Brown, A. G. A., Vallenari, A., Prusti, T., et al. 2016, A&A, 595, A2
Chabrier, G. 2003, PASP, 115, 763
de Laverny, P., Recio-Blanco, A., Worley, C. C., et al. 2013, Messenger, 153, 18
De Pascale, M., Worley, C. C., de Laverny, P., et al. 2014, A&A, 570, A68
Dotter, A., Chaboyer, B., Jevremovic, D., et al. 2008, ApJS, 178
Edvardsson, B., Andersen, J., Gustafsson, B., et al. 1993, A&A, 275, 101
Fuhrmann, K. 1998, A&A, 338, 161
Gilmore, G. & Reid, N. 1983, MNRAS, 202, 1025
Girardi, L., Groenewegen, M. A. T., Hatziminaoglou, E., & Da Costa, L. 2005, A&A, 436, 895
González Hernández, J. I. & Bonifacio, P. 2009, A&A, 497, 497
Guiglion, G., Recio-Blanco, A., de Laverny, P., et al. 2015, A&A, 583, A91
Hayden, M. R. 2017a, A&A, In Press
Hayden, M. R. 2017b, In Prep
Hayden, M. R., Bovy, J., Holtzman, J. A., et al. 2015, ApJ, 808, 132
Hayden, M. R., Holtzman, J. A., Bovy, J., et al. 2014, AJ, 147, 116
Haywood, M., Di Matteo, P., Lehnert, M. D., Katz, D., & Gómez, A. 2013, A&A, 560, A109
Haywood, M., Lehnert, M. D., Di Matteo, P., et al. 2016, A&A, 589, A66
Jofré, P., Das, P., Bertranpetit, J., & Foley, R. 2017, MNRAS, 467, 1140
Jørgensen, B. R. & Lindegren, L. 2005, A&A, 436, 127
Kordopatis, G., Wyse, R. F. G., Gilmore, G., et al. 2015, A&A, 582, A122
Lindegren, L., Lammers, U., Bastian, U., et al. 2016, A&A, 595, A4
Mackereth, J. T., Bovy, J., Schiavon, R. P., et al. 2017, MNRAS, 471, 3057
Masseron, T. & Gilmore, G. 2015, MNRAS, 453, 1855
Mikolaitis, Š., de Laverny, P., Recio-Blanco, A., et al. 2017, A&A, 600, A22
Minchev, I., Martig, M., Streich, D., et al. 2015, ApJL, 804, L9
Nidever, D. L., Bovy, J., Bird, J. C., et al. 2014, ApJ, 796, 38
Prusti, T., de Bruijne, J. H. J., Brown, A. G. A., et al. 2016, A&A, 595, A1
Recio-Blanco, A., Bijaoui, A., & De Laverny, P. 2006, MNRAS, 370, 141
Recio-Blanco, A., de Laverny, P., Kordopatis, G., et al. 2014, A&A, 567, A5
Rix, H.-W. & Bovy, J. 2013, A&ARv, 21, 61
Robin, A. C., Luri, X., Reylé, C., et al. 2012, A&A, 543, A100
Sellwood, J. A. & Binney, J. J. 2002, MNRAS, 336, 785
Yoshii, Y. 1982, PASJ, 34, 365

[1] Laboratoire Lagrange (UMR7293), Université de Nice Sophia Antipolis, CNRS, Observatoire de la Côte d'Azur, BP 4229, 06304 Nice Cedex 4, France (mhayden@oca.eu)
[2] Institute of Theoretical Physics and Astronomy, Vilnius University, Saulėtekio al. 3, LT-10257, Vilnius, Lithuania
[3] Institute of Astronomy, Cambridge University, Madingley Road, Cambridge CB3 0HA, UK

Appendix A Ages

As noted above, we used Bayesian inference to determine ages to individual stars by comparing derived stellar parameters to isochrones. The Dartmouth isochrones (Dotter et al. 2008) used have metallicities ranging from $-2.0 < [Fe/H] < 0.6$ in steps of 0.1 dex, are linearly spaced in age in steps of 100 Myr from 0.1 Gyr to 15 Gyr, and have [Mg/Fe] spacing of 0.2 dex from $0.0 < [Mg/Fe] < 0.4$. The isochrones and the AMBRE stellar parameters are on a slightly different temperature scale based on the V-K colors of the stars. We find an offset of 100K using the color-temperature relations derived in González Hernández & Bonifacio (2009) between the temperatures derived from AMBRE and those of the isochrones, and apply a shift of 100K to the T_{eff} to place the derived AMBRE temperatures on the same scale as the isochrone temperatures. A complete description of the method, along with a catalog of the ages presented in this paper, will be described in a later paper (Hayden 2017b).

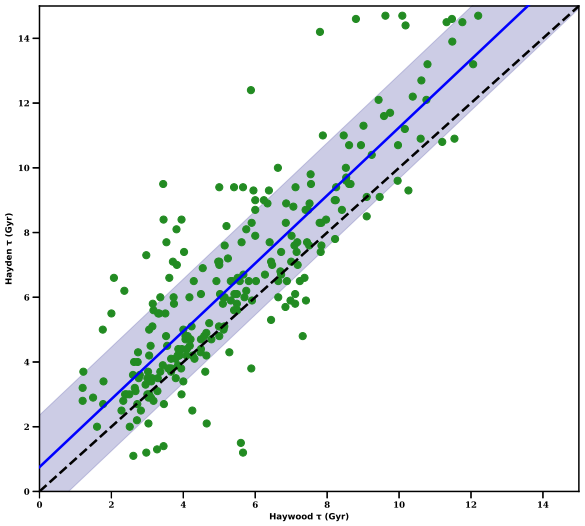

Fig. A.1. Comparison between our derived ages and those provided by Haywood et al. (2013). The dashed black line denotes the 1:1 relation, while the blue line denotes the relation between our derived ages and those of Haywood with a slope of 1.03. The blue shaded region shows the 1σ scatter of 1.6 Gyr.

To determine the stellar ages, we adopt several simple priors. We assume a uniform star formation history and additionally weight each isochrone point by mass using a Chabrier IMF (Chabrier 2003). No prior for age as a function of metallicity or [Mg/Fe] is used (i.e., we do not force a high-[Mg/Fe] or metal-poor star to be old). The mode of the generated PDF is used to characterize the age of an individual star. While carrying out tests with simulated observations using stars from TRILEGAL, we find ages are reliable (relative errors $< 1 - 2$ Gyr) for turnoff and subgiant stars only, which are selected by requiring $M_J < 3.75$ and $3.6 < \log g < 4.4$. From our initial sample of nearly 1,500 stars, 494 meet our selection criteria. Additionally, we compared these remaining stars to stars in common with (Haywood et al. 2013) as shown in Fig. A. We find a systematic offset of 1 Gyr, identical to the right panel of Fig. 3 of Haywood et al. (2013) when comparing their method using Dartmouth and Y^2 isochrones. Other than the systematic offset, the ages are very similar, with a linear 1:1 relation found between the age estimates and a random scatter of 1.6 Gyr between the samples, despite using independent stellar parameters, abundances, and isochrone sets. The largest outliers are driven primarily by differences in temperature between AMBRE and those adopted by Haywood et al. (2013). Additionally, for the oldest stars the different age ranges covered by the isochrones also has an impact.

MNRAS 000, 1–?? (2017) Preprint 13 December 2017 Compiled using MNRAS LATEX style file v3.0

The age-velocity dispersion relation of the Galactic discs from LAMOST-*Gaia* data

Jincheng Yu* & Chao Liu
National Astronomical Observatories, Chinese Academy of Sciences, Beijing 100012, China

Manuscript Version: Aug 2017

ABSTRACT

We present the age-velocity dispersion relation (AVR) in three dimensions in the solar neighbourhood using 3,564 commonly observed sub-giant/red-giant branch stars selected from LAMOST, which gives the age and radial velocity, and *Gaia*, which measures the distance and proper motion. The stars are separated into metal-poor ([Fe/H] < -0.2 dex and metal-rich ([Fe/H] > -0.2 dex) groups, so that the metal-rich stars are mostly α-poor, while the metal-poor group are mostly contributed by α-enhanced stars. Thus, the old and metal-poor stars likely belong to the chemically defined thick disc population, while the metal-rich sample is dominated by the thin disc. The AVR for the metal-poor sample shows an abrupt increase at $\gtrsim 7$ Gyr, which is contributed by the thick disc component. On the other hand, most of the thin disc stars with [Fe/H] > -0.2 dex display a power-law like AVR with indices of about 0.3–0.4 and 0.5 for the in-plane and vertical dispersions, respectively. This is consistent with the scenario that the disc is gradually heated by the spiral arms and/or the giant molecular clouds. Moreover, the older thin disc stars (> 7 Gyr) have a rounder velocity ellipsoid, i.e. σ_ϕ/σ_z is close to 1.0, probably due to the more efficient heating in vertical direction. Particularly for the old metal-poor sample located with $|z| > 270$ pc, the vertical dispersion is even larger than its azimuthal counterpart. Finally, the vertex deviations and the tilt angles are plausibly around zero with large uncertainties.

Key words: Galaxy: evolution – Galaxy: disc – Galaxy: kinematics and dynamics – solar neighbourhood

1 INTRODUCTION

The age-kinematics relation of the stars in the solar neighbourhood provides crucial information on the structure and evolution of the Milky Way. The velocity ellipsoid, as a descriptive quantity of the distribution function, for these stars reflects the gravitational potential and hence the spatial structure, while the varying kinematics with the stellar ages can constrain the evolution of the Galaxy.

Older stars are observed to have larger velocity dispersions (Casagrande et al. 2011), while younger stars are typically kinematically cool (Aumer & Binney 2009). The increasing trend of the velocity dispersions with age is known as the age-velocity dispersion relation (AVR) and has been discussed for decades (e.g. Strömberg 1946; Wielen 1977; Nordström et al. 2004). Quillen & Garnett (2001) detected a jump in the AVR for stars older than 9 Gyr from a sample of F and G dwarf stars and identified the jump as a thick disc component caused by minor merger. Other works favours a simple power law (Aumer & Binney 2009; Holmberg, Nordström, & Andersen 2009) with a saturation for stars older than 8 Gyr.

One possible explanation is that the stars are born with a decreasing velocity dispersion, since the turbulence of gas discs decreases with age due to the decreasing gas accretion rates (Bournaud, Elmegreen, & Martig 2009; Forbes, Krumholz, & Burkert 2012; Bird et al. 2013). Ma et al. (2017) found that stars older than 6 Gyr were formed in a violent mode, while stars younger than 6 Gyr were formed in a relatively calm disc in a cosmological zoom-in simulation. This view is also supported by observations of gas kinematics in disc galaxies which shows a decline of intrinsic velocity dispersion with decreasing redshift (Wisnioski et al. 2015). However, the observed clumpy galaxies might be too massive to be the progenitors of Milky Way-type galaxies (e.g. van Dokkum et al. 2013; Inoue & Saitoh 2014). Furthermore, it is unclear how the kinematics of young stars which form from cold gas relate to the observations.

Most theoretical works treated the observed AVR as a conse-

* email: yujc.astro@gmail.com

quence of gradual heating through scattering processes, with the assumption that stars are born with a roughly constant velocity dispersion probably smaller than 10 km s^{-1} (Aumer & Binney 2009). Both massive gas clouds (Spitzer & Schwarzschild 1953) and spiral arms (Barbanis & Woltjer 1967) are considered as scattering agents.

Sellwood & Carlberg (1984) and Carlberg & Sellwood (1985) showed that the transient spirals can significantly heat the in-plane motion of disc stars without much influence the vertical motion (e.g. Sellwood 2013; Martinez-Medina et al. 2015). However, the observed σ_z increases similarly with age as the in-plane components (Holmberg et al. 2009), implying that the spiral arms cannot be the only source.

Spitzer & Schwarzschild (1953) showed that giant molecular clouds (GMCs) with masses of $10^6 M_\odot$ can heat the disc. Lacey (1984) extended the work to three dimensions and found that GMCs are quite efficient at redirecting the velocity of stars out of the plane, but rather inefficient at increasing its amplitude.

As a secular heating source, the Galactic bar has also been discussed in the literature (Saha, Tseng & Taam 2010; Grand et al. 2016). However, although heating induced by the bar mainly takes place in the inner disc, the effect in the outer disc is not clear. Thus, the bar may contribute little to the observed AVR in the solar neighbourhood (Moetazedian & Just 2016).

Radial migration is another important mechanism in disc evolution (e.g. Sellwood & Binney 2002; Roškar et al. 2008; Schönrich & Binney 2009b; Minchev & Famaey 2010; Kordopatis et al. 2015), and has been proposed as a source of disc heating (e.g. Schönrich & Binney 2009a; Loebman et al. 2011; Roškar et al. 2013). As Sellwood & Binney (2002) and Solway, Sellwood & Schönrich (2012) pointed out, churning by spiral structures can redistribute the stars radially and hence causes far more mixing with very limited heating. Furthermore, Minchev et al. (2012) showed that the contribution of radial migration to the disc heating is negligible because of the balance between the outwards migrating stars, which 'heat' the disc, and inward migrating stars, which 'cool' it.

The shape of the velocity ellipsoid can also be associated with the heating processes providing that most of the stars are in equilibrium. Lacey (1984) concluded that GMC scattering should cause that the value of vertical dispersion (σ_z) is in between the radial (σ_R) and azimuthal (σ_ϕ) components. However, this is inconsistent with the observed flattened velocity ellipsoid, i.e., $\sigma_z < \sigma_\phi$ (Holmberg et al. 2009). Sellwood (2008), using simulations, clarified that Lacey's prediction neglected the perturbations from the distant encounters. Ida, Kokubo & Makino (1993) corrected Lacey's heating rate and predicted that the vertical dispersion is the smallest among the three dispersion components. Tian et al. (2015) showed that, for the stars located close to the Galactic mid-plane, vertical dispersion is the smallest component. Smith, Whiteoak & Evans (2012) found that although the shape of the velocity ellipsoid for the metal-rich stars is as expected, the ellipsoid for metal-poor stars is rounder, i.e., $\sigma_z > \sigma_\phi$.

Bovy et al. (2012) developed a "mono-abundance population" method (MAP) by analysing spatial structure for stars in small bins in [Fe/H] and [α/Fe] space. They found that the thick disc has larger scale height and smaller scale length than the thin disc. The distinct properties of the thick disc population were later confirmed by Bovy et al. (2016); Mackereth et al. (2017), using a similar method. Although these results well presented how chemical structural parameters of discs vary with abundance and age, the lack of a direct connection between age and velocity ellipsoids leads to an indirect way of exploring the dynamical evolution of the disc structures.

In this paper, we use sub-giant branch (SGB) and low red giant branch (RGB) stars to revisit the AVR in the solar neighbourhood. With the measured radial velocities and ages from The Large Sky Area Multi-Object Fiber Spectroscopic Telescope (LAMOST) survey (Cui et al. 2012) DR3 catalogue, combined with the parallaxes and proper motions from the Tycho-Gaia Astrometric Solution (TGAS; Gaia Collaboration et al. 2016), we are able to construct the age–kinematics relation within 1 kpc of the Sun, which for this purpose is the solar neighbourhood.

The paper is organized as follows. In Section 2, we describe our data and the methods to derive the age and the velocity ellipsoid. Then we show the main result in Section 3, and discuss the result in Section 4. Our final conclusion is given in Section 5.

2 THE SAMPLES

2.1 The LAMOST SGB/RGB stars

LAMOST survey has well observed a few 10^5 K giant stars (Liu et al. 2014). Recent studies showed that they can be used as age tracers (Martig et al. 2016). For LAMOST K giant stars, Ho et al. (2017b) have provided ages for about 230,000 of them. However, because we want to use the accurate proper motions provided by TGAS, most of these K giant stars are located beyond 1 kpc. Consequently, they are either not included in the TGAS catalogue or do not have reliable astrometric measurements.

Therefore, following Liu et al. (2015), we use the SGB/RGB stars as the age tracers. Specifically, stars with $5000 < T_{\rm eff} < 5300$ K and $3 < \log g < 4$ dex are selected for age estimation. The SGB stars and the low RGB stars (located at the base of the red giant branch) can well separate the age older than 1 Gyr in $T_{\rm eff}$–$\log g$ plane. The SGB stars with ages younger than 1 Gyr are difficult to isolate because they are located at larger $T_{\rm eff}$ and smaller $\log g$ and hence may be contaminated by horizontal-branch stars. Compared to the turn-off stars, another group of age tracers, the selected SGB/RGB samples are less affected by the main-sequence stars, fast-rotating stars, blue stragglers, and binaries.

2.2 The age estimation

We adopt the method to estimate the age for the SGB/RGB stars provided by Liu et al. (2015). We compare the LAMOST pipeline (Wu et al. 2011, 2014) provided stellar parameters of these stars, $T_{\rm eff}$, $\log g$, and [Fe/H], with PARSEC isochrones (Bressan et al. 2012). The isochrones have a denser grid in logarithmic age ($\Delta \log a = 0.01$) and metallicity (Δ[Fe/H] = 0.1) with the coverage of $4950 \leqslant T_{\rm eff} \leqslant 5350$ and $2.9 \leqslant \log g \leqslant 4.1$.

For the ith star, the likelihood that it has stellar parameter set O_i=($T_{{\rm eff},i}$, $\log g_i$, [Fe/H]$_i$) given age τ, initial mass $\mathcal{M}_{\rm ini}$, and absolute magnitude M can be written as

$$L_i(O_i|\tau, \mathcal{M}_{\rm ini}, M) = \exp\left(-\sum_{k=1}^{3} \frac{(O_{i,k} - T_k(\tau, \mathcal{M}_{\rm ini}, M))^2}{2\sigma_{i,k}^2}\right), \quad (1)$$

where $T_k(\tau, \mathcal{M}_{\rm ini}, M))$ is the predicted stellar parameter set (k = 1, 2, and 3 correspond to $T_{{\rm eff},i}$, $\log g_i$, or $[{\rm Fe/H}]_i$, respectively) from isochrones and $\sigma_{i,k}$ the uncertainty of the observed stellar parameters. As the nuisance parameters, $\mathcal{M}_{\rm ini}$ and M are marginalized and leave τ as the only unknown parameter.

Liu et al. (2015) assessed the performance of the age estimates with the test mock data and concluded that 1) the typical random error of the age is about 30% and 2) it may be underestimated by at most 2 Gyr when the age estimate is larger than 8 Gyr. Therefore, we adopt 30% uncertainty as the age estimate for all the sample stars.

2.3 The Sample Selection

61,134 SGB/RGB stars following the selection criteria mentioned in section 2.1 are selected from LAMOST DR3, which in total contains more than 4 million stellar spectra with stellar parameters been estimated. The accuracy of the radial velocity of LAMOST is better than 5 km s^{-1} (Gao et al. 2014) with a systematic offset of 5.7 km s^{-1} according to Tian et al. (2015).

As part of GAIA survey DR1 (Gaia Collaboration et al. 2016), the TGAS catalogue provides parallaxes and proper motions for about 2 million stars down to the 12th mag. The uncertainty of the proper motions is about 1 mas yr^{-1}, while the typical uncertainty for the parallaxes is 0.3 mas including systematic errors.

We cross-match the LAMOST SGB/RGB stars with TGAS catalogue and obtain a sample of 3,564 common stars with age estimates. Following Liu et al. (2017), the LAMOST targets are selected purely based on their photometry. The TGAS selection effect correction is mostly due to uneven spatial distribution coverage in the 14 month *Gaia* data release. Therefore, both surveys have a negligible selection effects in the kinematics.

Because the distance directly converted from the inverse of the parallax may be significantly overestimated for stars farther than 500 pc, we adopt the distance derived from Astraatmadja & Bailer-Jones (2016), who applied a Bayesian method to the distance estimation from the parallax with the Milky Way prior. Note that the systematic bias of the TGAS astrometry has been applied twice unintentionally by the authors (Bailer-Jones private communication). This may induce about 1.5 km s^{-1} in the uncertainty of the velocity. However, such a small value may not substantially change the velocity ellipsoids since the measurement uncertainty is contributed as a squared term in the latter quantities.

Figure 1 shows the vertical spatial distribution of the sample, which roughly spans to $|z| \sim 1000$ pc, allowing for the comparison of the kinematics at different vertical heights.

2.4 Likelihood function

We adopt cylindrical coordinates to decompose the stellar motion into radial, azimuthal and vertical velocity components. The position of the Sun is adopted as $(X, Y, Z) = (8000, 0, 27)$ pc, while the solar motion with respect to the local standard of rest (LSR) is adopted as $(U_\odot, V_\odot, W_\odot) = (9.58, 10.52, 7.01)$ km s^{-1} (Tian et al. 2015).

We assume that the velocity distribution in the disc can be modelled as a multivariate Gaussian distribution, but note that the distribution of the azimuthal component need not be a Gaussian. Tian et al. (2015) found that the Gaussian approximation does not induce significant systematic bias in the estimation of the velocity ellipsoid. Thus, the likelihood function can be constructed such as

$$L = \prod_{i=1}^{N} \frac{1}{(2\pi)^{\frac{n}{2}} |\mathbf{\Sigma}|^{\frac{1}{2}}} \exp\left(-\frac{1}{2}(\boldsymbol{v}-\boldsymbol{\mu})^T \mathbf{\Sigma}^{-1} (\boldsymbol{v}-\boldsymbol{\mu})\right), \quad (2)$$

where $\mathbf{\Sigma}$ is the squared sum of the intrinsic velocity tensor and the covariance matrix of the uncertainty of the velocity estimates and $\boldsymbol{\mu}$ represents for $(v_{\rm R}, v_\phi, v_z)^T$ in the Galactocentric cylindrical coordinates. $\boldsymbol{\mu}$ and the terms related to the intrinsic velocity ellipsoid in $\mathbf{\Sigma}$ are the parameters to be determined. We choose the prior of the velocity dispersions to be uniformly distributed in the range of $(0, +\infty)$. Note that the uncertainties of the observed line-of-sight velocity ($\approx$ 5 km s^{-1}), the proper motions, and the Bayesian distances have been taken into account when computing $\mathbf{\Sigma}$. Eq. 2 is equivalent to the case that the measurement uncertainties are deconvolved from the measured dispersions so that the intrinsic velocity ellipsoid would not be broadened by the measurement errors.

We estimate the mean velocities and the velocity ellipsoids for a given stellar population using the Markov chain Monte Carlo (MCMC) simulation with the *emcee* package (Foreman-Mackey et al. 2013).

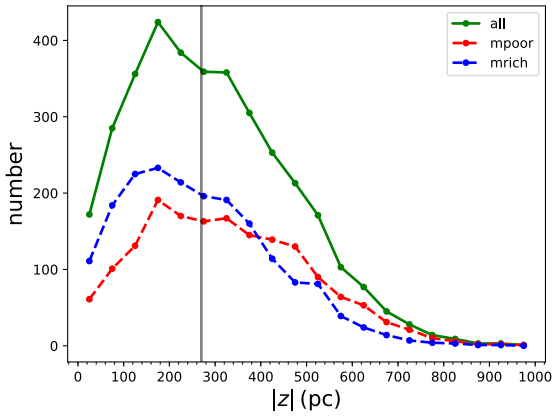

Figure 1. The vertical spatial distribution of the SGB/RGB star samples. The green line represents for the distribution for the whole sample, while the red and blue lines stand for the distributions for the sample with [Fe/H] < −0.2 dex and [Fe/H] > −0.2 dex, respectively. The black vertical line indicates the point of $|z|$ = 270 pc to separate the data into two roughly equal number sub-groups (see the text for details).

3 RESULTS

3.1 Separations in $|z|$ and age

The distribution of the sample in the vertical height $|z|$ is displayed in Figure 1. It has a broad distribution with a peak located at around 100-200 pc. The largest vertical distance for the sample reaches to about 1000 pc. This range of $|z|$ allows for the detection of both the thin and thick discs. In order to compare the AVR at different heights, the samples are divided into two different $|z|$ bins such that each $|z|$ bin contains similar number of stars. The sample with $|z|$ <

270 pc has 1,775 stars, while the sample with $|z| > 270$ pc has 1,789 stars.

The stars located in each $|z|$ bin are split into various age bins. Table 1 and 2 list the age bins for the whole dataset, the metal-rich sample, and the metal-poor sample (the definition of the two metallicity separated samples can be found in section 3.2) at $|z| < 270$ pc and $|z| > 270$ pc, respectively. The principle to split the data into age bins is that the width of any age bin should be 30% around its central value according to the uncertainty of the age estimates (Liu et al. 2015). Meanwhile, the centre points of the neighbouring age bins should be separated by at least 15% of the age value. Furthermore, the number of stars in each age bin is set to be between 100 and 400. Consequently, the neighbouring age bins may overlap with each other, which smooth the resulting velocity ellipsoids such that the arbitrarily fluctuation in the AVR can be reduced.

3.2 Separations in metallicity

The stellar populations can be well characterized by the stellar age, metallicity, and α-abundance. The kinematical features for the populations with various ages, metallicities, and α-abundance may hint at the dynamical evolution of the discs. However, for the data in this work, the number of stars in each age bin is set to be between 100 and 400 to meet the requirement of statistical significance of the kinematics with enough age resolution. Within each age bin, the number of stars may not be sufficient for further dividing into many metallicity bins. Moreover, not all of the sample stars, but only about two thirds have [α/Fe] been estimated (Ho et al. 2017a). Therefore, we decide to only separate the data into two sub-groups in [Fe/H] so that the variation of the AVR can be still investigated for the chemically-defined thin/thick disc. The chemical definition of the thin and thick discs is usually based on [α/Fe]. The stars with larger [α/Fe] are likely from the thick disc population, while those with smaller [α/Fe] are likely from the thin disc. The separation point is usually selected at around [α/Fe] $\sim$ 0.2 dex (Lee et al. 2011).

Figure 2 shows the age–[Fe/H]–[α/Fe]–$|z|$ relationship for a subset of 2,139 stars, which contain [Fe/H] and [α/Fe] measurements by Ho et al. (2017a), from the whole 3,564 SGB/RGB star sample. Ho et al. (2017a) estimated the chemical abundances by cross-calibrating the LAMOST DR2 K giant stars with APOGEE data by applying *The Cannon* technique. As expected, it shows a clear bimodality with a gap at around [α/Fe] $\sim$ 0.15 - 0.2 dex. Following the criterion for [α/Fe] from previous works (Lee et al. 2011; Liu & van de Ven 2012), we could separate the sample into α-enhanced and -poor populations to represent the chemically-defined thick and thin discs. However, because [α/Fe] is not estimated for about one third of our samples, we have looked for an alternative criterion for the thin/thick disc separation to take the place of [α/Fe].

We find that the two discs can be at least partly disentangled using [Fe/H] = −0.2 dex. On one hand, stars with [Fe/H] > −0.2 dex are only composed of those with [α/Fe] $\lesssim$ 0.2 dex, i.e. only the chemically-defined thin disc contributes to this sub-group. On the other hand, the sample with [Fe/H] < −0.2 dex contains both α-poor and α-enhanced stars, implying that this sub-group may reflect the kinematical features for both thin and thick discs.

It is noted that, as shown in the middle panel of the figure, the stars with [α/Fe] $\gtrsim$ 0.2 dex from the metal-"poor" ([Fe/H] < −0.2) sub-group (red dots) dominate the regime of age > 7 Gyr, while those with [α/Fe] $\lesssim$ 0.2 dex are mostly 4 to 8 Gyr old. Hence, the metal-poor sub-sample can be separated into two parts: 1) those with age $\gtrsim$ 7 Gyr are dominated by the thick disc population; 2) those with age $\lesssim$ 7 Gyr should be thin disc stars mostly older than 3 Gyr. Meanwhile, the metal-"rich" ([Fe/H] > −0.2) sub-group (blue dots) is prominent in the range of age < 8 Gyr with few stars extending to older age. This means that the chemically-defined thin disc can be traced by the metal-rich stars in the whole range of age. Therefore, although the separation at [Fe/H] = −0.2 dex is not perfect for disentangling the thin and thick discs, the significant difference in the distribution in the age–[α/Fe] plane for the two sub-groups is sufficient in investigating the different AVRs for the thin and thick discs. In the rest of the paper, we treat the metal-poor sub-sample with age $\gtrsim$ 7 Gyr as the tracer of the chemically-defined thick disc and treat the metal-rich sub-sample as the probe of the thin disc population.

Finally, the right panel of the figure shows that both the metal-poor and metal-rich sub-sample are broadly distributed in both $|z| <$ 270 and > 270 pc. Hence the AVR at different vertical heights for both sub-sample can be compared.

In the rest of this paper, we use [Fe/H] derived from LAMOST data pipeline. As shown in Figure 3, the difference of [Fe/H] between Ho et al. (2017a) and the LAMOST pipeline is mostly within 0.1 dex. Therefore, we can still use [Fe/H]= −0.2 dex to separate the samples into metal-poor and -rich sub-groups.

3.3 The resulting AVRs

For each $|z|$ and [Fe/H] bin, the 3-dimensional velocity ellipsoids for the populations with various ages are determined with the MCMC simulation. The diagonal components of the velocity ellipsoids, i.e. σ_R, σ_ϕ, and σ_z, as functions of age for each $|z|$ and [Fe/H] bin are displayed in different panels of Figure 4. Meanwhile, the velocity dispersions, their ratios, the vertex deviations, and the tilt angles are listed in Table 1 and 2 for stars located at $|z| <$ 270 and > 270 pc, respectively.

The left hand panels of Figure 4 show the trends of σ_R, σ_ϕ, and σ_z with age from top to bottom, respectively, for $|z| <$ 270 pc. Looking at the velocity dispersions for the two sub-samples (red dots for metal-poor stars and blue stars for metal-rich), all of the three dispersions increase with age. This is consistent with previous works (e.g. Bournaud et al. 2009; Holmberg et al. 2009; Smith et al. 2012; Tian et al. 2015). However, the increasing rates with age for the two sub-samples are significantly different. Firstly, the red dots, which represent the metal-poor sub-group stars, show plateaus of velocity dispersions substantially larger than those for the metal-rich stars for age $\gtrsim$ 7 Gyr. They are more significant in σ_ϕ and σ_z than in σ_R. For the metal-poor stars, σ_ϕ is between 34 and 43 km s^{-1} for age $\gtrsim$ 7 Gyr, while it is only around 24 $\sim$ 26 km s^{-1} for the metal-rich stars at the same ages. Similarly, for the metal-poor stars, σ_z is around 34 $\sim$ 38 km s^{-1} for age $\gtrsim$ 7 Gyr, while for the metal-rich stars, the value is only at 18 $\sim$ 23 km s^{-1}. Since the metal-poor sub-sample with age $\gtrsim$ 7 Gyr is dominated by the chemically-defined thick disc, it seems that the significant differences are caused by the different kinematical features between the thick and thin disc. Secondly, for age < 7 Gyr, velocity dispersions for the metal-poor sub-sample and those for metal-rich sub-sample are quite similar.

Table 1. Kinematical features for stars with $|z| < 270$ pc at various age bins.

Age (Gyr)	N	σ_r (km s^{-1})	σ_ϕ (km s^{-1})	σ_z (km s^{-1})	σ_r/σ_ϕ	σ_r/σ_z	σ_ϕ/σ_z	l_v (deg)	α (deg)
			all stars						
1.4 ± 0.3	100	21.7 ± 2.0	12.5 ± 1.5	8.2 ± 1.1	1.7 ± 0.3	2.7 ± 0.4	1.5 ± 0.3	7.3 ± 7.4	−1.1 ± 3.8
1.9 ± 0.3	100	21.6 ± 2.0	17.1 ± 1.6	10.3 ± 1.1	1.3 ± 0.2	2.1 ± 0.3	1.7 ± 0.2	0.1 ± 16.5	9.7 ± 5.0
2.3 ± 0.2	100	24.7 ± 2.1	18.9 ± 1.8	10.6 ± 1.1	1.3 ± 0.2	2.3 ± 0.3	1.8 ± 0.2	11.3 ± 12.9	2.7 ± 3.9
2.6 ± 0.2	115	31.2 ± 2.4	18.6 ± 1.7	10.8 ± 1.1	1.7 ± 0.2	2.9 ± 0.4	1.7 ± 0.2	1.0 ± 6.3	−3.6 ± 2.9
3.1 ± 0.2	152	31.9 ± 2.1	17.5 ± 1.4	12.3 ± 1.0	1.8 ± 0.2	2.6 ± 0.3	1.4 ± 0.2	5.3 ± 4.7	−1.6 ± 2.8
3.6 ± 0.3	233	32.8 ± 1.7	18.7 ± 1.0	13.8 ± 0.9	1.8 ± 0.1	2.4 ± 0.2	1.3 ± 0.1	6.4 ± 3.8	−0.7 ± 2.4
4.1 ± 0.3	391	32.4 ± 1.3	19.8 ± 0.8	14.1 ± 0.7	1.6 ± 0.1	2.3 ± 0.1	1.4 ± 0.1	4.9 ± 3.5	−2.7 ± 1.8
4.5 ± 0.3	400	34.9 ± 1.4	20.5 ± 0.9	14.1 ± 0.6	1.7 ± 0.1	2.5 ± 0.1	1.5 ± 0.1	9.3 ± 2.9	−0.2 ± 1.6
5.0 ± 0.3	400	37.5 ± 1.5	22.2 ± 0.9	16.8 ± 0.7	1.7 ± 0.1	2.2 ± 0.1	1.3 ± 0.1	9.2 ± 2.9	2.4 ± 1.9
5.5 ± 0.4	400	38.4 ± 1.5	22.8 ± 1.0	19.5 ± 0.8	1.7 ± 0.1	2.0 ± 0.1	1.2 ± 0.1	3.3 ± 2.9	1.5 ± 2.3
6.1 ± 0.5	361	43.0 ± 1.8	24.8 ± 1.1	21.2 ± 0.9	1.7 ± 0.1	2.0 ± 0.1	1.2 ± 0.1	2.4 ± 3.0	−3.0 ± 2.2
7.0 ± 0.5	257	47.5 ± 2.2	28.9 ± 1.6	24.5 ± 1.3	1.6 ± 0.1	1.9 ± 0.1	1.2 ± 0.1	6.9 ± 3.9	−3.6 ± 2.8
8.0 ± 0.6	169	50.6 ± 3.0	32.8 ± 2.1	29.2 ± 2.0	1.5 ± 0.1	1.7 ± 0.2	1.1 ± 0.1	11.7 ± 5.2	−2.3 ± 4.3
9.5 ± 0.7	157	51.7 ± 3.3	36.4 ± 2.4	34.2 ± 2.2	1.4 ± 0.1	1.5 ± 0.1	1.1 ± 0.1	−5.0 ± 7.2	−2.2 ± 5.8
10.2 ± 0.5	100	56.7 ± 4.3	35.3 ± 3.0	37.8 ± 3.0	1.6 ± 0.2	1.5 ± 0.2	0.9 ± 0.1	1.8 ± 6.6	5.1 ± 7.3
			[Fe/H] > −0.2 dex						
1.4 ± 0.4	100	21.7 ± 1.9	12.0 ± 1.4	8.6 ± 1.1	1.8 ± 0.3	2.5 ± 0.4	1.4 ± 0.2	7.4 ± 6.8	−0.6 ± 3.9
1.9 ± 0.3	100	21.4 ± 1.9	16.7 ± 1.6	10.1 ± 1.1	1.3 ± 0.2	2.1 ± 0.3	1.7 ± 0.2	17.8 ± 13.1	2.4 ± 4.8
2.4 ± 0.2	100	27.8 ± 2.5	18.9 ± 1.7	10.5 ± 1.1	1.5 ± 0.2	2.6 ± 0.4	1.8 ± 0.2	−2.8 ± 9.0	−0.3 ± 3.2
2.8 ± 0.2	100	32.7 ± 2.7	18.4 ± 1.7	11.0 ± 1.2	1.8 ± 0.2	3.0 ± 0.4	1.7 ± 0.2	0.2 ± 5.7	0.5 ± 2.8
3.3 ± 0.2	132	31.3 ± 2.3	16.8 ± 1.4	11.9 ± 1.0	1.9 ± 0.2	2.6 ± 0.3	1.4 ± 0.2	12.6 ± 4.7	1.7 ± 2.9
3.8 ± 0.3	196	30.1 ± 1.6	16.9 ± 1.1	11.7 ± 0.8	1.8 ± 0.1	2.6 ± 0.2	1.4 ± 0.1	6.7 ± 4.0	1.2 ± 2.4
4.3 ± 0.3	277	34.7 ± 1.6	17.8 ± 0.9	12.6 ± 0.7	2.0 ± 0.1	2.8 ± 0.2	1.4 ± 0.1	9.7 ± 2.9	−1.7 ± 1.6
4.9 ± 0.4	304	36.8 ± 1.7	21.2 ± 1.0	16.8 ± 0.8	1.7 ± 0.1	2.2 ± 0.1	1.3 ± 0.1	11.2 ± 3.1	−1.5 ± 2.1
5.6 ± 0.4	255	39.3 ± 2.0	22.1 ± 1.1	17.7 ± 0.9	1.8 ± 0.1	2.2 ± 0.2	1.3 ± 0.1	6.0 ± 3.2	−0.3 ± 2.4
6.4 ± 0.5	188	42.5 ± 2.5	23.0 ± 1.3	18.3 ± 1.1	1.8 ± 0.1	2.3 ± 0.2	1.3 ± 0.1	4.2 ± 3.7	−3.0 ± 2.7
7.2 ± 0.5	106	43.8 ± 3.3	24.2 ± 2.0	23.3 ± 1.7	1.8 ± 0.2	1.9 ± 0.2	1.0 ± 0.1	3.0 ± 5.0	−3.2 ± 4.6
8.5 ± 0.8	57	51.8 ± 5.6	25.8 ± 2.9	23.3 ± 2.6	2.0 ± 0.3	2.2 ± 0.3	1.1 ± 0.2	2.0 ± 5.6	6.2 ± 4.9
			[Fe/H] < −0.2 dex						
3.2 ± 0.6	100	29.8 ± 2.4	19.0 ± 1.9	13.8 ± 1.3	1.6 ± 0.2	2.2 ± 0.3	1.4 ± 0.2	6.9 ± 7.8	−7.4 ± 4.3
3.8 ± 0.3	100	31.3 ± 2.5	19.7 ± 1.8	14.8 ± 1.4	1.6 ± 0.2	2.1 ± 0.3	1.3 ± 0.2	2.0 ± 7.2	−5.6 ± 4.3
4.5 ± 0.3	168	35.2 ± 2.1	21.1 ± 1.4	16.1 ± 1.1	1.7 ± 0.2	2.2 ± 0.2	1.3 ± 0.1	1.5 ± 4.8	3.4 ± 2.9
5.0 ± 0.4	224	38.2 ± 2.1	21.0 ± 1.2	17.3 ± 1.1	1.8 ± 0.1	2.2 ± 0.2	1.2 ± 0.1	2.3 ± 3.5	4.1 ± 2.6
5.7 ± 0.4	196	39.8 ± 2.4	23.7 ± 1.4	22.1 ± 1.3	1.7 ± 0.1	1.8 ± 0.2	1.1 ± 0.1	−1.5 ± 4.4	2.7 ± 3.8
6.4 ± 0.5	135	43.6 ± 3.1	30.0 ± 2.3	27.9 ± 2.1	1.5 ± 0.2	1.6 ± 0.2	1.1 ± 0.1	−0.1 ± 7.8	−4.1 ± 5.9
7.6 ± 0.6	106	53.4 ± 4.4	42.5 ± 4.0	33.9 ± 2.8	1.3 ± 0.2	1.6 ± 0.2	1.3 ± 0.2	26.8 ± 9.4	−11.0 ± 6.6
8.9 ± 0.8	116	56.5 ± 4.2	37.8 ± 3.0	35.4 ± 2.6	1.5 ± 0.2	1.6 ± 0.2	1.1 ± 0.1	3.7 ± 7.5	−3.7 ± 6.4
10.1 ± 0.6	110	56.5 ± 4.1	34.3 ± 2.5	37.5 ± 2.8	1.6 ± 0.2	1.5 ± 0.2	0.9 ± 0.1	−0.4 ± 6.1	6.1 ± 7.1

These trends can also be seen from Table 1. Finally, at around 2-3 Gyr, both σ_R and σ_ϕ show an abrupt jump-up, which is not obviously seen in σ_z at the same age.

The right hand panels of Figure 4 display the AVRs for the three velocity dispersions for $|z| > 270$ pc. Almost all the differences between the metal-poor and metal-rich sub-groups shown in the lower vertical height in the left panels are found in the sample for $|z| > 270$ kpc. For the metal-rich sub-sample, the trends of σ_R, σ_ϕ and σ_z are quite similar with those for $|z| < 270$ pc. In other words, σ_R, σ_ϕ and σ_z do not show significant vertical gradients in the metal-rich sub-sample. The values of σ_R and σ_ϕ for the metal-poor sub-sample are also quite similar on both side of $|z| = 270$ pc. However, the values of σ_z for age $\gtrsim$ 7 Gyr and $|z| > 270$ pc are significantly larger than those with similar ages but $|z| < 270$ pc for the metal-poor sample.

4 DISCUSSION

4.1 Thin and thick discs

As shown in Figure 4, the significant difference in velocity dispersions between the metal-rich and metal-poor sub-samples for age $\gtrsim$ 7 Gyr indicates that the chemically-defined thick disc (traced by the meta-poor sub-samples with age $\gtrsim$ 7 Gyr) has distinct kinematic features, i.e. it is hotter than the old thin disc stars (traced by the metal-rich sub-samples) in all three velocity dispersions, especially in vertical direction. This implies that although the heating of the thin disc leads to a relatively larger σ_z, i.e. makes it thicker, at early time, it can not produce such a large σ_z plateau as the chemically-defined thick disc. Therefore, it seems that the chemically-defined thick disc should be a distinct population to the heated old thin disc. Note that, for age $\gtrsim$ 7 Gyr, our age estimates may suffer from larger systematics as well as larger uncertainties (Liu et al. 2015), hence the lower age limit for the thick disc could be slightly larger than 7 Gyr.

Moreover, it is noted that although the thick disc traced by the metal-poor sub-sample with age $\gtrsim$ 7 Gyr shows large difference in

Table 2. Kinematical features for stars with $|z| > 270$ pc at various age bins.

Age (Gyr)	N	σ_r (km s^{-1})	σ_ϕ (km s^{-1})	σ_z (km s^{-1})	σ_r/σ_ϕ	σ_r/σ_z	σ_ϕ/σ_z	l_v (deg)	α (deg)
			all stars						
1.6 ± 0.4	100	26.4 ± 2.3	12.5 ± 1.5	10.5 ± 1.2	2.1 ± 0.3	2.5 ± 0.4	1.2 ± 0.2	−0.4 ± 5.4	9.0 ± 4.3
2.2 ± 0.3	100	28.8 ± 2.6	13.2 ± 1.5	14.9 ± 1.4	2.2 ± 0.3	1.9 ± 0.3	0.9 ± 0.1	−3.8 ± 5.1	13.0 ± 5.5
2.7 ± 0.3	100	29.2 ± 2.7	13.7 ± 1.5	15.7 ± 1.5	2.1 ± 0.3	1.9 ± 0.2	0.9 ± 0.1	0.8 ± 4.9	8.9 ± 6.1
3.1 ± 0.2	121	28.9 ± 2.4	15.6 ± 1.5	15.8 ± 1.3	1.8 ± 0.2	1.8 ± 0.2	1.0 ± 0.1	8.5 ± 5.0	−3.2 ± 5.2
3.6 ± 0.3	187	27.1 ± 1.9	17.7 ± 1.3	14.5 ± 1.0	1.5 ± 0.2	1.9 ± 0.2	1.2 ± 0.1	12.2 ± 5.8	1.2 ± 4.1
4.1 ± 0.3	280	27.6 ± 1.5	17.6 ± 1.0	16.3 ± 0.8	1.6 ± 0.1	1.7 ± 0.1	1.1 ± 0.1	4.7 ± 4.7	10.2 ± 3.8
4.7 ± 0.3	400	30.8 ± 1.3	17.0 ± 0.9	17.1 ± 0.8	1.8 ± 0.1	1.8 ± 0.1	1.0 ± 0.1	−1.4 ± 2.7	4.3 ± 2.9
5.2 ± 0.3	400	33.4 ± 1.5	18.6 ± 0.9	17.3 ± 0.8	1.8 ± 0.1	1.9 ± 0.1	1.1 ± 0.1	1.5 ± 2.8	3.7 ± 2.4
5.7 ± 0.3	400	33.8 ± 1.5	20.2 ± 1.0	20.2 ± 0.8	1.7 ± 0.1	1.7 ± 0.1	1.0 ± 0.1	3.3 ± 3.3	4.8 ± 3.1
6.3 ± 0.4	400	36.6 ± 1.7	21.9 ± 1.0	27.0 ± 1.0	1.7 ± 0.1	1.4 ± 0.1	0.8 ± 0.0	4.6 ± 3.3	8.8 ± 5.6
7.1 ± 0.6	365	42.1 ± 1.9	27.8 ± 1.4	33.6 ± 1.4	1.5 ± 0.1	1.3 ± 0.1	0.8 ± 0.1	5.9 ± 4.4	8.9 ± 7.3
8.0 ± 0.6	284	45.3 ± 2.4	31.8 ± 1.8	35.1 ± 1.7	1.4 ± 0.1	1.3 ± 0.1	0.9 ± 0.1	4.3 ± 5.7	−3.0 ± 8.0
9.3 ± 0.7	187	52.7 ± 3.4	32.0 ± 2.2	38.8 ± 2.3	1.6 ± 0.2	1.4 ± 0.1	0.8 ± 0.1	8.0 ± 5.0	−0.4 ± 7.9
10.3 ± 0.4	92	64.1 ± 5.8	35.0 ± 3.6	47.0 ± 4.0	1.8 ± 0.3	1.4 ± 0.2	0.7 ± 0.1	6.5 ± 6.1	−5.1 ± 10.9
			[Fe/H] > −0.2 dex						
1.6 ± 0.5	100	26.8 ± 2.4	10.8 ± 1.3	11.3 ± 1.3	2.5 ± 0.4	2.4 ± 0.3	1.0 ± 0.2	−1.2 ± 4.3	10.5 ± 4.4
2.4 ± 0.4	100	30.2 ± 2.7	12.6 ± 1.4	14.9 ± 1.4	2.4 ± 0.3	2.0 ± 0.3	0.8 ± 0.1	2.1 ± 4.4	8.1 ± 5.2
3.0 ± 0.3	100	28.1 ± 2.6	15.1 ± 1.5	14.0 ± 1.3	1.9 ± 0.3	2.0 ± 0.3	1.1 ± 0.1	9.1 ± 5.6	3.5 ± 5.1
3.5 ± 0.3	122	25.9 ± 2.2	16.4 ± 1.4	12.2 ± 1.1	1.6 ± 0.2	2.1 ± 0.3	1.3 ± 0.2	14.2 ± 6.7	−3.1 ± 4.1
4.1 ± 0.3	167	27.1 ± 1.9	16.6 ± 1.2	15.4 ± 1.1	1.6 ± 0.2	1.8 ± 0.2	1.1 ± 0.1	13.0 ± 5.1	7.7 ± 4.7
4.6 ± 0.3	216	27.4 ± 1.7	17.3 ± 1.1	16.2 ± 1.0	1.6 ± 0.1	1.7 ± 0.1	1.1 ± 0.1	9.4 ± 4.9	8.5 ± 4.4
5.3 ± 0.4	247	31.0 ± 1.7	18.3 ± 1.1	17.7 ± 0.9	1.7 ± 0.1	1.8 ± 0.1	1.0 ± 0.1	4.3 ± 4.1	3.3 ± 3.7
5.9 ± 0.4	217	34.9 ± 2.1	19.8 ± 1.2	20.0 ± 1.1	1.8 ± 0.1	1.7 ± 0.1	1.0 ± 0.1	−0.1 ± 3.8	3.0 ± 3.8
6.7 ± 0.6	131	38.9 ± 2.9	23.8 ± 1.9	23.2 ± 1.7	1.6 ± 0.2	1.7 ± 0.2	1.0 ± 0.1	0.4 ± 5.5	0.1 ± 5.5
8.0 ± 0.8	100	41.5 ± 3.4	28.5 ± 2.5	24.8 ± 2.0	1.5 ± 0.2	1.7 ± 0.2	1.1 ± 0.1	12.1 ± 8.3	3.1 ± 6.0
8.9 ± 0.6	47	44.7 ± 5.5	29.6 ± 3.8	23.2 ± 3.0	1.5 ± 0.3	1.9 ± 0.3	1.3 ± 0.2	21.6 ± 9.7	9.2 ± 7.6
			[Fe/H] < −0.2 dex						
3.1 ± 0.7	100	28.2 ± 2.7	18.6 ± 2.0	17.0 ± 1.6	1.5 ± 0.2	1.7 ± 0.2	1.1 ± 0.2	1.2 ± 9.0	8.4 ± 7.1
3.9 ± 0.3	100	29.0 ± 2.7	19.1 ± 2.0	19.2 ± 1.7	1.5 ± 0.2	1.5 ± 0.2	1.0 ± 0.1	3.4 ± 8.7	5.0 ± 8.5
4.6 ± 0.3	168	34.3 ± 2.3	17.1 ± 1.4	18.1 ± 1.3	2.0 ± 0.2	1.9 ± 0.2	0.9 ± 0.1	−6.2 ± 3.8	0.9 ± 4.1
5.2 ± 0.4	224	35.9 ± 1.8	18.6 ± 1.2	18.7 ± 1.0	1.9 ± 0.2	1.9 ± 0.1	1.0 ± 0.1	−0.7 ± 3.1	3.4 ± 3.1
5.8 ± 0.4	196	36.4 ± 1.8	20.7 ± 1.1	24.2 ± 1.1	1.8 ± 0.1	1.5 ± 0.1	0.9 ± 0.1	5.1 ± 3.5	13.2 ± 4.6
6.7 ± 0.5	135	41.2 ± 2.3	26.9 ± 1.7	32.8 ± 1.7	1.5 ± 0.1	1.3 ± 0.1	0.8 ± 0.1	6.2 ± 5.4	8.1 ± 8.8
7.5 ± 0.6	106	44.5 ± 2.7	31.9 ± 2.3	39.5 ± 2.2	1.4 ± 0.1	1.1 ± 0.1	0.8 ± 0.1	8.0 ± 7.4	1.2 ± 18.6
8.6 ± 0.7	116	51.3 ± 3.6	33.1 ± 2.7	44.2 ± 2.7	1.6 ± 0.2	1.2 ± 0.1	0.7 ± 0.1	−1.5 ± 6.6	11.4 ± 16.4
10.1 ± 0.6	110	62.8 ± 4.9	37.4 ± 3.3	47.0 ± 3.7	1.7 ± 0.2	1.3 ± 0.1	0.8 ± 0.1	5.6 ± 6.3	0.1 ± 10.5

σ_z with the thin disc, its σ_R and σ_ϕ are only moderately larger than the thin disc with similar age.

Comparing σ_ϕ for $|z| < 270$ with that at $|z| > 270$ pc, σ_ϕ does not change very much at different heights for the thick disc stars, while it increases from $\sim$ 25 km s^{-1} to about $\sim$ 30 km s^{-1} for the thin disc sub-sample with age $\gtrsim$ 7 Gyr. This implies that the thick disc should be formed on relatively smaller time scale such that the whole population shows similar velocity dispersion, while the thin disc may be formed on a longer time scale and thus the secular dynamical evolution can play some role to heat and scatter the older stars to a larger range of height.

Finally, for the metal-poor sub-sample with age < 7 Gyr, because the chemically-defined thin disc dominates in these data, the stars essentially show similar AVRs to the metal-rich sub-sample in all three components.

Although the significantly different velocity dispersions shown in AVR can separate the thick from the thin disc, this remains insufficient for discriminating the origin of the thick disc. Using cosmological simulations, Martig, Minchev, & Flynn (2014) found that galaxies commonly undergo an active phase of mergers at high redshift, creating a thick stellar component. In this scenario, the oldest stars with age > 9 Gyr are born kinematically hot.

4.2 Heating in the disc

At lower redshift, Martig et al. (2014) showed that the vertical velocity dispersion (σ_z) increases smoothly with age. They suggested that the disc heating is mainly contributed by disc growth and a combination of spiral arms and bars coupled with overdensities in the disc and vertical bending waves. The heating mechanisms lead to a power-law like AVR, while the active phase of mergers at high redshift breaks the power-law like AVR with age > 9 Gyr. The authors pointed out that the jumps in AVR may also be created by mergers (also see House et al. 2011). However, they found that errors of 30% in stellar ages can significantly blur the signatures of mergers. Therefore, we apply the power-law relation to the chemically-defined thin disc component.

We fit the AVR for the metal-rich stars within 3 Gyr - 9 Gyr using a power-law relation. The samples not in the range of age suffers from larger uncertainties due to the smaller numbers in these age bins. The best-fit models of the AVR for the metal-rich populations are shown in Figure 5. The derived AVRs in all three directions are well represented by a power-law when the youngest and oldest bins are excluded.

The derived power indices for the radial dispersions for $|z| <$

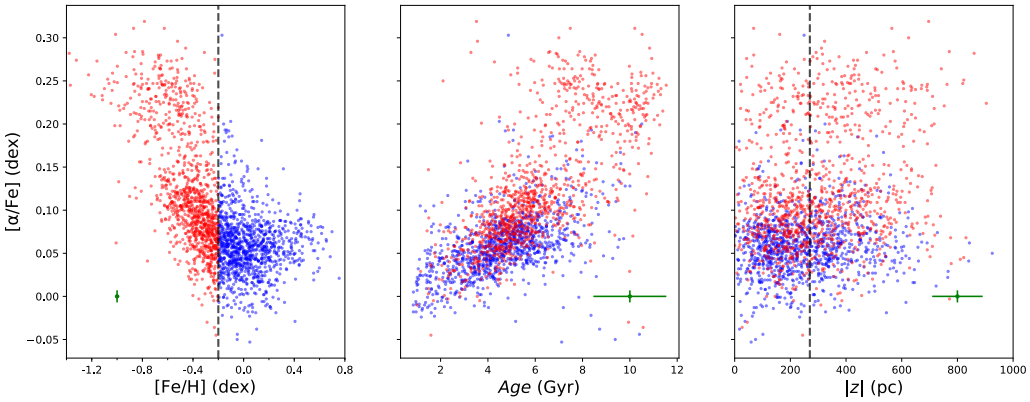

Figure 2. [α/Fe]-[Fe/H] relation (left panel), [α/Fe]-age relation (middle panel) and [α/Fe]-$|z|$ relation (right panel) for part of (2,139 stars) our sample (3,564 stars). In the left panel, the vertical black dashed line at [Fe/H] = −0.2 dex gives the dividing criterion for the metal-poor and metal-rich populations. The metal-poor population is dominated by α-enhanced star, while most of stars in the metal-rich population have lower α-abundance. The middle panel shows that the α-enhanced stars are mostly old, while α-poor stars spread in a wide range of age. The right panel shows that both metal-poor and metal-rich populations distribute broadly in vertical direction, at both sides of $|z|$ = 270 pc, which is indicated by the vertical dashed line. The green error bars in each panel give the corresponding median uncertainties of the sample. Note that the median uncertainty of [Fe/H] is 0.02 dex, which is almost invisible in the plot.

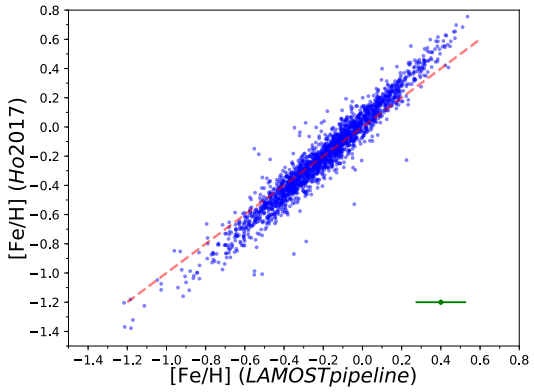

Figure 3. The [Fe/H] derived by (Ho et al. 2017a) (labeled as Ho2017) versus the [Fe/H] from LAMOST pipeline (labeled as LAMOST pipeline). The red dashed line shows the 1 : 1 relation. The green errorbar gives the median uncertainties.

270 and $|z| > 270$ pc are $\beta = 0.34 \pm 0.17$ and $\beta = 0.39 \pm 0.13$, respectively, while for the azimuthal direction we obtain $\beta = 0.34 \pm 0.12$ and $\beta = 0.42 \pm 0.14$. The derived power indices for the vertical direction, which are $\beta = 0.56 \pm 0.14$ and $\beta = 0.51 \pm 0.15$, are higher than the other two directions. The radial and azimuthal velocity dispersion are approximately coupled by the relation:

$$\frac{\sigma_R}{\sigma_\phi} = \frac{\kappa}{2\Omega}, \quad (3)$$

where κ and Ω are the epicycle frequency and the azimuthal frequency for nearly circular orbits in the solar neighbourhood (Binney & Tremaine 2008). Thus, the in-plane power indices are expected to be similar. Furthermore, the in-plane power indices at high-$|z|$ are slightly higher than that in low-$|z|$, indicating that the heating sources might be more scattered to higher-$|z|$. Nevertheless, all these in-plane power indices are around 0.3-0.4, while the vertical power indices are around 0.5, which is consistent with other works (e.g. Aumer & Binney 2009; Holmberg et al. 2009).

We conclude that the AVR of the metal-rich population is consistent with heating mechanisms via scattering processes mainly induced by spiral arms and GMCs.

Note that the resulting $\boldsymbol{\sigma}$ for the thin disc are systematically higher than the fitted power-law at age > 7 Gyr. This could be because that the older populations are more affected by larger uncertainties from the age estimates. According to Liu et al. (2015), the ages can be underestimated by at most 2 Gyr in the old regime. Then the old stars with larger velocity dispersions may be merged to the bins of slightly younger age. As a result, the slope of the age-σ relation at the old age regime becomes steeper. An alternative reason may be that the heating process is not constant on long time scales. Considering that the number density of GMCs was significantly higher in the past than in the present day (Chiappini, Matteucci, & Gratton 1997), older stars may therefore be more efficiently scattered in the early time. It is also possible that the more frequent mergers at high redshift can affect the velocity dispersion.

4.3 σ-ratio

The velocity dispersion ratios of our sample are shown in Figure 6. There is no substantial trend in the ratio σ_R/σ_ϕ with age. The result is consistent with the theoretical expectation that the ratio σ_R/σ_ϕ is a constant since they are coupled (see Eq. 3). On the other hand,

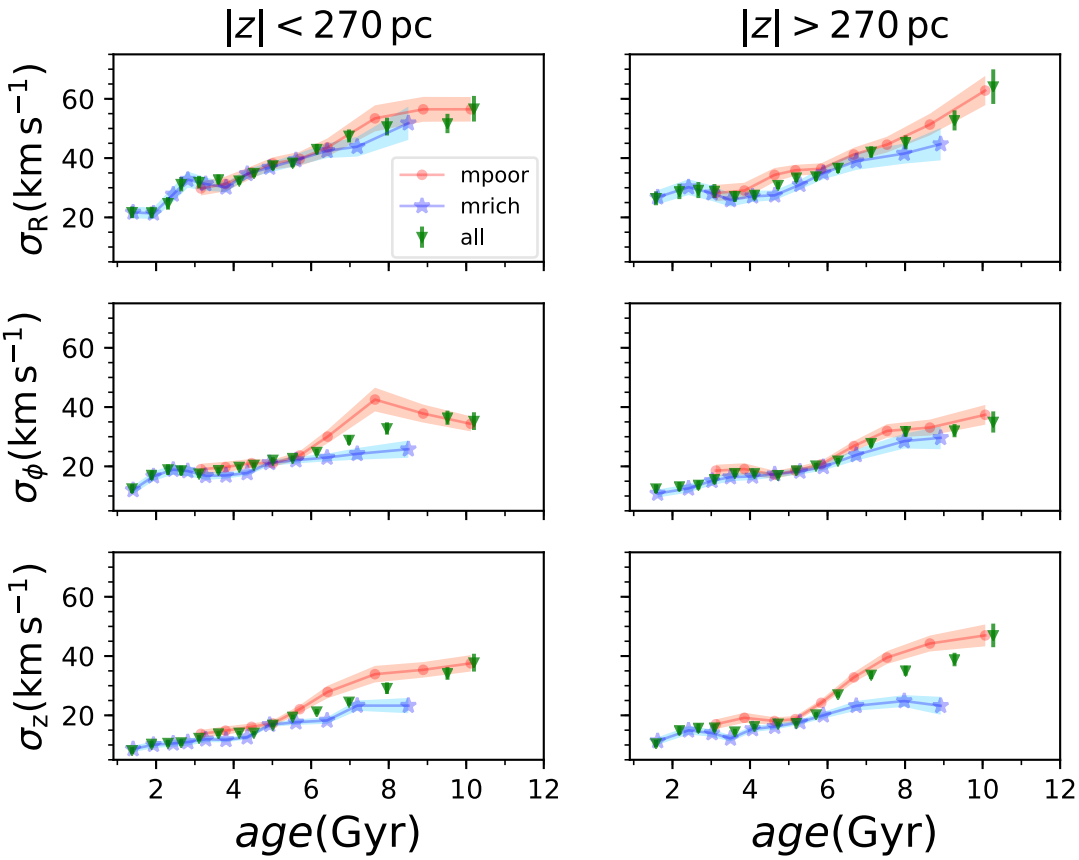

Figure 4. The AVR for the two sub-samples with different metallicities at two different $|z|$ bins. Different coloured symbols represent different samples. The green triangles represent the whole sample, labelled as "all". The red dots represent the metal-poor sample, labelled as "mpoor". The blue stars represent the metal-rich sample, labelled as "mrich". The red and blue shaded bands give the corresponding errors for the metal-poor and metal-rich sample, respectively.

because the stars are more efficiently heated in vertical direction, as can be inferred from the larger power indices in vertical direction, the ratios of in-plane to vertical dispersions decrease with age.

Previous observations show that the vertical dispersion σ_z is smallest among the three components. Lacey (1984) analysed the scattering by GMCs and predicted that the value of σ_z should be in between σ_R and σ_ϕ. Ida et al. (1993) later found that Lacey (1984) overestimated the vertical heating rate while underestimated the radial heating rate. They predicted that the vertical component should be the smallest although precise shape depends on the local slope of the rotation curve. Their expectations are confirmed by simulations by Shiidsuka & Ida (1999). Sellwood (2008), using simulations, pointed out that the ratio σ_ϕ/σ_z depends on the distant GMCs, that is, when enough distant GMC perturbations are taken into account, σ_z generally remains the smallest of the velocity dispersions.

However, we find that the ratio $\sigma_\phi/\sigma_z \approx 1$ for stars with $|z| > 270$ pc. Moreover, it drops below 1 for metal-poor stars with $|z| > 270$ pc. In other words, the vertical dispersion for the metal-poor stars at higher-$|z|$ is larger than the azimuthal dispersion. Holmberg et al. (2009) showed a flattened shape of velocity ellipsoid with σ_z to be the smallest, although the ratio σ_z/σ_ϕ increases with age. Smith et al. (2012) confirmed a similar velocity ellipsoid shape for the metal-rich stars ([Fe/H] $\geqslant -0.5$ dex). However, they found that the value of σ_z is in between the other two for the metal-poor stars ([Fe/H] < -0.5 dex), which is very similar to our result. Tian et al. (2015) also reported that vertical velocity dispersion values are in the middle for stars with $T_{\rm eff} \sim 6500$ K at $300 < |z| < 500$ pc, which are likely dominated by the old turn-off thick disc stars. Therefore, it is likely that the ratio $\sigma_\phi/\sigma_z < 1$ is due to the distinct kinematic feature of the dominating old thick disc population.

4.4 Vertex deviation and tilt angle

The covariances (or the cross-terms) of the velocity ellipsoid reflects the tilts of the ellipsoid, which is associated with the non-axisymmetric structures in the Galactic gravitational potential.

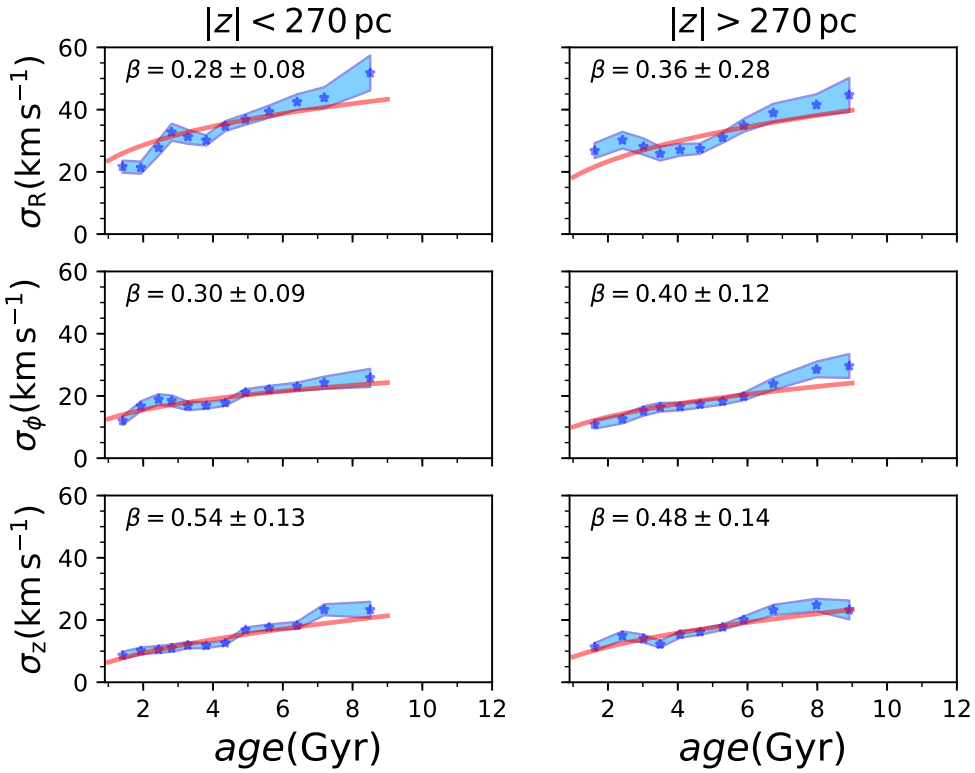

Figure 5. AVRs at different vertical heights for metal-rich population ([Fe/H] > −0.2 dex). Blue stars show the derived velocity dispersion in different age-bins, while the blue shaded bands indicates the corresponding errors. The red solid curve shows the best fit power law for bins with age between 3 Gyr and 9 Gyr.

They are usually quantified by tilt angle, which is the deviation from the R − z plane, and vertex deviation, which is the deviation from the R − ϕ plane, for convenience. The definition of vertex deviation is:

$$l_{\rm v} \equiv \frac{1}{2}\arctan\left(\frac{2\sigma^2_{\rm R\phi}}{\sigma^2_{\rm R}-\sigma^2_{\phi}}\right), \quad (4)$$

and the definition of the tilt angle is:

$$\alpha \equiv \frac{1}{2}\arctan\left(\frac{2\sigma^2_{\rm Rz}}{\sigma^2_{\rm R}-\sigma^2_{\rm z}}\right). \quad (5)$$

The derived vertex deviation and the tilt angle at various age bins are shown in Figure 7. The vertex deviations at different vertical heights are plausibly zero for all stars but with large uncertainties. Dehnen & Binney (1998) showed the vertex deviation as a function of colour index. The stars with $B - V > 0.4$ were found to have vertex deviation at around 10° with a 5° uncertainty, while the stars with $B - V < 0.4$ have vertex deviation around 20°–30° with an error between 2.8° and 5.3°. Smith et al. (2012) reported similar results for the metal-rich stars ([Fe/H] $\geqslant -0.5$ dex). They also found that the vertex deviation is around 0° for metal-poor stars but with large uncertainty. Tian et al. (2015) found that the vertex deviations are around 0° with an error between 5° and 10° for different effective temperatures at different |z|, although they found it can be as large as ∼ 27° for stars with $T_{\rm eff} < 4500$ K at 300 < |z| < 500 pc, yet the uncertainty is as large as ∼ 14°.

The tilt angle of our sample is around 0° for most of the stars but the measurement has very large uncertainties. Tian et al. (2015) found the tilt angle to be around 0° with an error of ∼ 5°, while Smith et al. (2012) reported a non-zero α to be around 10° with an uncertainty of ∼ 10°. Siebert et al. (2008) used red clump giants from the Radial Velocity Experiment (RAVE) survey and gave a tilt angle of 7.3° ± 1.8° at $z \sim 1$ kpc below the plane. Büdenbender, van de Ven, & Watkins (2015) used G-dwarfs which spans a large vertical range, reaching as far as 3 kpc, and found an increasing trend of tilt angle with |z| in the range of 0° − 15° with a 10° uncertainty.

5 CONCLUSIONS

In this paper, we use 3,564 SGB/RGB stars selected from LAMOST DR3 and TGAS data to derive the AVR in the solar neighbourhood. By dividing the samples into two sub-groups with [Fe/H] < −0.2 dex and [Fe/H] > −0.2 dex, we are able to compare the AVR between the thin and thick discs. We find that:

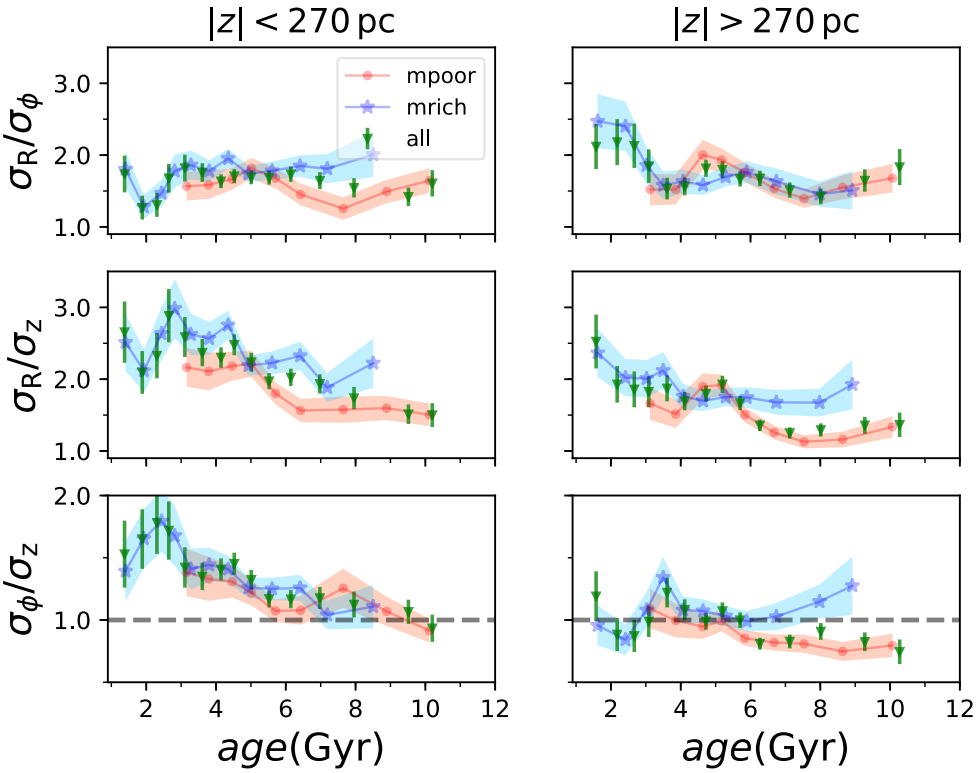

Figure 6. Ratios of velocity dispersion at different vertical heights. Green triangles show the ratio for the whole sample. The red dots and blue stars with shaded errors correspond to stars with [Fe/H] < −0.2 dex (metal-poor) and [Fe/H] > −0.2 dex (metal-rich), respectively.

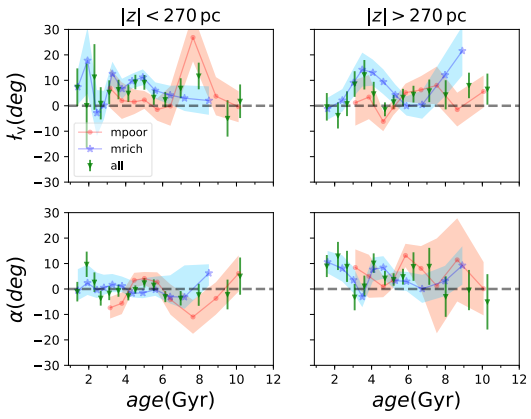

Figure 7. The vertex deviation and the tilt angle as functions of age at different vertical heights. Green triangles show the ratio for the whole sample. The red dots and blue stars with shaded errors correspond to stars with [Fe/H] < −0.2 dex (metal-poor) and [Fe/H] > −0.2 dex (metal-rich), respectively.

(i) the large difference in the AVR between the metal-poor and metal-rich sample at age $\gtrsim$ 7 Gyr favours that the chemically-defined thick disc is a distinct population formed within a short time scale, which is different from the thin disc.

(ii) the AVR for the metal-rich stars follows a power-law with best-fit indices between 0.3 and 0.4 for in plane velocity dispersions and around 0.5 for vertical dispersion. This is consistent with secular heating of the thin disc which is mainly driven by spiral arms and GMCs. As Casagrande et al. (2011) and Aumer, Binney, & Schönrich (2016) point out, large age uncertainties can flatten the AVR, therefore the intrinsic increasing rate of velocity dispersion should be higher.

(iii) $\sigma_R/\sigma_z < 1$ for the old metal-poor stars, which belong to the thick disc. For the metal-rich stars, which are mostly from the thin disc, the in-plane to vertical dispersion ratios decrease with age but remain > 1 for the oldest stars.

(iv) the vertex deviations and the tilt angles are plausibly around zero, but with large uncertainties.

ACKNOWLEDGMENTS

We thank Christopher Flynn for the detailed and constructive review, which improved the paper a lot. This work is supported by the

National Key Basic Research Program of China 2014CB845700. C.L. acknowledges the National Natural Science Foundation of China (NSFC) under grants 11373032 and 11333003. Guoshoujing Telescope (the Large Sky Area Multi-Object Fiber Spectroscopic Telescope LAMOST) is a National Major Scientific Project built by the Chinese Academy of Sciences. Funding for the project has been provided by the National Development and Reform Commission. LAMOST is operated and managed by the National Astronomical Observatories, Chinese Academy of Sciences.

REFERENCES

Astraatmadja T. L., Bailer-Jones C. A. L., 2016, ApJ, 833, 119
Aumer M., Binney J. J., 2011, MNRAS, 397, 1286
Aumer M., Binney J., Schönrich, R., 2016, MNRAS, 462, 1697
Barbanis B., Woltjer L., 1967, ApJ, 150, 461
Binney J., Tremaine S., 2008, Galactic Dynamics, 2nd edn. Princeton Univ. Press, Princeton, NJ
Bird J. C., Kazantzidis S., Weinberg D. H., Guedes J., Callegari S., Mayer L., Madau P., 2013, ApJ, 773, 43
Bournaud F., Elmegreen B. G., Martig M., 2009, ApJ, 707, L1
Bovy J., Rix H.-W., Liu C., Hogg D. W., Beers T. C., Lee Y. S. 2012, ApJ, 753, 148
Bovy J., Rix H.-W., Schlafly E. F., Nidever D. L., Holtzman J. A., Shetrone M., Beers T. C., 2016, ApJ, 823, 30
Bressan A., Marigo P., Girardi L., Salasnich B., Dal Cero C., Rubele S., Nanni A., 2012, MNRAS, 427, 127
Büdenbender A., van de Ven G., Watkins L. L. 2015, MNRAS, 452, 956
Casagrande L., Schönrich R., Asplund M., Cassisi S., Ramírez I., Meléndez J., Bensby T., Feltzing S., 2011, A&A, 530, A138
Carlberg R. G., Sellwood J. A., 1985, ApJ, 292, 79
Chiappini C., Matteucci F., Gratton R., 1997, ApJ, 477, 765
Cui X.-Q., et al., 2012, RAA, 12, 1197
Dehnen W., Binney J. J., 1998, MNRAS, 298, 387
Forbes J., Krumholz M., Burkert A., 2012, ApJ, 754, 48
Foreman-Mackey D., Hogg D. W., Lang D., Goodman J., 2013, PASP, 125, 306
Gaia Collaboration, Brown A. G. A., et al., 2016, A&A, 595, A2
Gao S., Liu C., Zhang X., Justham S., Deng L., Yang M., 2014, ApJ, 788, 37
Goodman J., Weare J., 2010, Commun. Appl. Math. Comput. Sci., 5, 65
Grand R. J. J., Springel V., Gómez F. A., Marinacci F., Pakmor R., Campbell D. J. R., Jenkins A., 2016, MNRAS, 459, 199
Haywood M., Di Matteo P., Lehnert M. D., Katz D., Gómez A., 2013, 560, A109
Ho A. Y. Q., Ness M. K., Hogg D. W., Rix H., Liu C., Yang F., Zhang Y., Hou Y., Wang Y., 2017, ApJ, 836, 5
Ho A. Y. Q., Rix H.-W., Ness M. K., Hogg D. W., Liu C., Ting Y.-S., 2017, ApJ, 841, 40
House E. L., et al., 2011, MNRAS, 415, 2652
Holmberg J., Nordström B., Andersen J., 2009, A&A, 501, 941
Ida S., Kokubo E., Makino J., 1993, MNRAS, 263, 875
Inoue S., Saitoh T. R., 2014, MNRAS, 441, 243
Kordopatis G., et al., 2015, MNRAS, 447, 3526
Kuijken K., Gilmore G., 1989, MNRAS, 239, 571
Lacey C. G., 1984, MNRAS, 208, 687
Lee Y. S., et al., 2011, ApJ, 738, 187
Liu C., van de Ven G., 2012, MNRAS, 425, 2144
Liu C., et al., 2014, ApJ, 790, 110
Liu C., et al., 2015, ArXiv e-prints, arXiv:1510:06123
Liu C., et al., 2017, Research in Astronomy and Astrophysics, 17, 96
Loebman S. R., Roškar R., Debattista V. P., Ivezić Ž., Quinn T. R., Wadsley J., 2011, ApJ, 737, 8
Ma X, Hopkins P. F., Wetzel A. R., Kirby E. N., Anglés-Alcázar D., Faucher-Giguère C., Kereš D., Quataert E., 2017, MNRAS, 467, 2430
Mackereth J. T., et al., 2017, MNRAS, 471, 3057
Martig M., Minchev I., Flynn C., 2014, MNRAS, 443, 2452
Martig M., et al., 2016, MNRAS, 456, 3655
Martinez-Medina L. A., Pichardo B., Pérez-Villegas A., Moreno E., 2015, ApJ, 802, 109
Minchev I., Famaey B., 2010, ApJ, 722, 112
Minchev I., et al., 2012, A&A, 548, 126
Moetazedian R., Just A., 2016, MNRAS, 459, 2905
Nordström B., Mayor M., Andersen J., et al., 2004, A&A 418, 989
Quillen A. C., Garnett D. R., 2001, in Funes J. G., & Corsini E. M., eds, ASP, Conf. Ser. Vol. 230, Galaxy Disks and Disk Galaxies. Astron. Soc. Pac., San Francisco, p. 87
Roškar R., Debattista V. P., Quinn T. R., Stinson G. S., Wadsley J., 2008, ApJ, 684, L79
Roškar R., Debattista V. P., Loebman S. R., 2013, MNRAS, 433, 976
Saha K., Tseng Y.-H., Taam R. E., 2010, ApJ, 721, 1878
Schönrich R., Binney J., 2009, MNRAS, 396, 203
Schönrich R., Binney J., 2009, MNRAS, 399, 1145
Sellwood J. A., Carlberg R. G., 1984, ApJ, 282, 61
Sellwood J. A., Binney J. J., 2002, MNRAS, 336, 785
Sellwood J. A., 2008, in Funes J. G., & Corsini, E. M., eds, ASP, Conf. Ser. Vol. 396, Formation and Evolution of Galaxy Disks, Astronomical Society of the Pacific, San Francisco, p. 341
Sellwood J. A., 2013, ApJ, 769, L24
Shiidsuka K., Ida, S., 1999, MNRAS, 307, 737
Siebert A., et al., 2008, MNRAS, 391, 793
Smith M. C., Whiteoak S. H., Evans N. W., 2012, ApJ, 746, 181
Soderblom D. R., 2010, ARA&A, 48, 581
Solway M., Sellwood J. A., Schönrich R., 2012, MNRAS, 422, 1363
Spitzer L. Jr., Schwarzschild M., 1953, ApJ, 118, 106
Strömberg G., 1946, ApJ, 104, 12
Tian H., et al., 2015, ApJ, 809, 145
van Dokkum P. G., et al., 2013, ApJ, 771, L35
Wielen R., 1977 A&A, 60, 263
Wisnioski E., et al., 2015, ApJ, 799, 209
Wu Y., et al., 2011, RAA, 11, 924
Wu Y., Du B., Luo A., Zhao Y., Yuan H., 2014, IAUS, 306, 340